FINAL RESEARCH SUBMISSION

HYPERLOOP **UPV**

Contents

List of Figures

List of Tables

Chapter 1

General

1.1 Description of the Team & Development Environment

Hyperloop UPV is a student team founded and based in Valencia, Spain, at the Universitat Politècnica de València —UPV—. Over its nine-year history, the team has shown consistent dedication to intensive research and innovation in the field of Hyperloop technology.

With 42 members from all university faculties, Hyperloop UPV embraces a multidisciplinary and collaborative approach to problem-solving. The team is structured into specialized working groups, or subsystems, each focusing on specific aspects of Hyperloop development. This structure allows the team to effectively tackle current challenges by drawing on a wide range of expertise. The team's skillset spans multiple disciplines, including engineering and operations management, ensuring a comprehensive and integrated approach to developing solutions.

Hyperloop UPV's main objectives are to design a scalable and functional vehicle capable of levitating within a vacuum-sealed tube, always prioritizing three core principles: safety, scalability, and sustainability.

The team benefits from the support of over 90 private and public entities. This backing makes it possible to bring the project to life year after year through vital in-kind or financial contributions.

With this research, titled *"Study and Comparison of Powering Methods for a real Hyperloop Vehicle"*, developed by Álvaro Martínez, Miquel Montañana, Gonzalo Sánchez and Marcos Pérez. Hyperloop UPV applies for the Full-Scale Award: Technical Aspects of Hyperloop Systems.

The total word count is 19,984 words.

Chapter 2

Abstract

The development of energy supply systems for Hyperloop technology represents one of the most critical and complex challenges in advancing future high-speed transport. Ensuring reliable, efficient, and scalable solutions is essential for meeting the demanding requirements of this new mode of transport, while also addressing key factors such as sustainability, technological maturity, and integration feasibility.

This study explores and compares various power supply alternatives applicable to a real-scale Hyperloop vehicle, providing a detailed analysis of different architectures and their potential for practical implementation. The work covers the design, simulation, and evaluation of multiple systems, including both external and on-board solutions, with the aim of identifying the technical, operational, and economic implications of each option.

By delivering a structured and objective framework for comparing energy supply technologies, this research contributes to the body of knowledge required to turn Hyperloop from a conceptual innovation into a viable and efficient transportation system. The insights provided are intended to support future developments in the field and encourage continued investigation into the optimization of energy systems for next-generation high-speed vehicles.

Chapter 3

Introduction

3.1 Motivation

The development of an adequate power supply system for a real Hyperloop vehicle represents one of the greatest challenges faced by engineering applied to high-speed transportation. A system capable of reaching speeds of up to 700 km/h in a sealed environment, without the possibility of drawing energy from external sources during the journey, requires an innovative energy solution that combines reliability, efficiency, and integration capability. The energy demand per trip is around 2 MWh, with power peaks reaching 24 MW during acceleration phases, which further increases the complexity of the design.

To address this challenge, this work presents the study, design, and comparison of three power supply systems potentially applicable to a real Hyperloop: a resonant LLC multistage supercharger, an inductive charging system, and a hydrogen fuel cell system. The first two are designed to supply an on-board battery, while the hydrogen system is proposed as a hybrid architecture combining fuel cells with a support battery, seeking a balance between autonomy and operational flexibility.

This study covers the technical sizing of each system, the analysis of their main components, the estimation of associated costs, and the evaluation of their technical and economic viability. The aim is to provide a clear and objective overview of the actual possibilities of each alternative, contributing to the development of a technology capable of meeting the demands of a future Hyperloop system. Ultimately, it seeks to provide a tool to compare solutions and support the design of a power supply system that combines efficiency, sustainability, and industrial feasibility.

3.2 Related Work

The development of power supply systems for Hyperloop vehicles is an emerging research field, with a limited number of studies due to the experimental nature of this technology. However, there are relevant works that have explored various energy solutions applicable to this type of transport.

In the field of battery-based systems and superchargers, several studies have focused on the design of high-power converters and the optimization of electrical architectures to minimize charging times,

including works on resonant LLC converters applied to fast charging in railway and electric vehicle contexts.

Inductive charging has been extensively studied for conventional electric vehicles and magnetic levitation —MAGLEV— trains, although its adaptation to Hyperloop introduces new challenges regarding power levels, efficiency, and infrastructure costs.

Hydrogen fuel cell systems have a more established track record in heavy transport and railway sectors, with studies addressing hybrid architectures with batteries, the integration of pressurized tanks, and the management of reactants and by-products — all key aspects for their potential application in a Hyperloop ecosystem.

This study builds on these precedents to propose, size, and compare solutions tailored to the specific requirements of this innovative transport system.

3.3 Research Objectives

The main objective of this work is to analyze, design, and compare different power supply solutions for a real Hyperloop vehicle, capable of meeting an energy demand of approximately 2 MWh per trip and power peaks of up to 24 MW during acceleration phases. To achieve this, three alternative systems are proposed: a resonant LLC multistage supercharger, an inductive charging system, and a hydrogen-based system in a hybrid configuration.

The specific objectives guiding this study are:

• To technically size each proposed system, defining its main components and integration within the Hyperloop ecosystem.

• To analyze and simulate the critical elements of each solution, validating their energy performance, efficiency, and supply capacity against the defined requirements.

• To estimate the implementation cost of each system, considering both the required infrastructure and the economic impact on train operation.

• To compare the proposed solutions from a technical, economic, and feasibility perspective, aiming to provide an objective framework for selecting the most suitable power supply system.

With this, the study seeks to lay the foundation for the development of an energy architecture capable of meeting the challenges posed by a high-speed transport system like Hyperloop, contributing to the advancement of this technology.

Chapter 4

Methodology

4.1 Overview

This work aims to design, size, and compare different energy solutions for a real Hyperloop system, targeting an energy demand of approximately 2 MWh per trip and power peaks of up to 24 MW during acceleration. Three technological alternatives have been studied: a resonant LLC multistage supercharger, an inductive charging system, and a hybrid hydrogen fuel cell and battery system.

For the resonant LLC multistage supercharger, a complete design of the converter has been carried out, including the sizing of its resonant tank, and its operation has been simulated in LTSpice using only commercial components. Various operating conditions have been analyzed, evaluating system efficiency, losses, thermal behavior of the devices, and technical feasibility. The study is complemented by a detailed economic analysis estimating implementation costs.

In the hydrogen-based system, the pressurized tanks required to store hydrogen, oxygen, and the water produced have been dimensioned. Different scenarios have been proposed and compared according to the maximum installed hydrogen power, analyzing the weights, occupied volumes, and associated costs in each configuration. This has made it possible to assess the flexibility and impact of the installed power on the vehicle's architecture.

For the inductive charging system, the design and simulation of the receiver coil system —pick-ups— have been carried out using JMAG software. Different geometric configurations and operating conditions have been analyzed to optimize power induction, magnetic flux uniformity, and overall system efficiency. A thermal study of the main components and an economic analysis estimating the total implementation cost of this technology have also been conducted.

Finally, the work includes an objective comparison of the three proposed solutions, considering parameters such as technological maturity, energy efficiency, system scalability, estimated costs, the impact of on-board weight, and required infrastructure. The aim is to provide a reference framework to support the selection of the most suitable power supply system for a future real Hyperloop.

4.2 Energy consumption for a Hyperloop Vehicle

In order to design various power supply systems for a real Hyperloop vehicle, it is essential to determine the energy demand that must be met. To achieve this, common initial conditions have been defined to ensure the study is as fair and comparable as possible. This analysis focuses on a Hyperloop vehicle with a capacity for 200 passengers, operating along a 500 km route at a cruising speed of 700 km/h. The journey is divided into three main phases: acceleration, cruise, and braking.

Given the early stage of development of the Hyperloop ecosystem, and its status as an experimental technology, reliable technical data remain scarce due to the limited number of companies working on its implementation worldwide. For this reason, some configurations in this study take as reference the proposal of "Hardt Hyperloop," a Netherlands-based company aiming to lead in the comprehensive development of this technology. In recent years, Hardt has made significant progress, including the construction of full-scale prototypes. The company'sIn order to design various power supply systems for a real Hyperloop vehicle, it is essential to determine the energy demand that must be met. To achieve this, common initial conditions have been defined to ensure the study is as fair and comparable as possible. This analysis focuses on a Hyperloop vehicle with a capacity for 200 passengers, operating along a 500 km route at a cruising speed of 700 km/h. The journey is divided into three main phases: acceleration, cruise, and braking.

Given the early stage of development of the Hyperloop ecosystem, and its status as an experimental technology, reliable technical data remain scarce due to the limited number of companies working on its implementation worldwide. For this reason, some configurations in this study take as reference the proposal of "Hardt Hyperloop," a Netherlands-based company aiming to lead in the comprehensive development of this technology. In recent years, Hardt has made significant progress, including the construction of full-scale prototypes. The company's website details various technical specifications of its commercial Hyperloop concept [12].

The decision to define a scenario with a 200-passenger train is based on the average capacity of conventional high-speed trains, typically around 300–400 passengers. However, Hardt's proposal considers a configuration for just 40 passengers. This study adopts an intermediate value of 200 passengers as a representative reference, balancing operational realism with technical demand.

The route is designed without intermediate stops, creating a more demanding scenario for the power supply systems, as they must ensure continuous energy delivery throughout the journey. Selecting a distance of 500 km allows for a connection between several major strategic cities. The table below presents some potential routes between cities over this distance:

Cities	Distance (km)
Madrid – Valencia	500
Paris – Lyon	500
Berlin – Munich	500
Milan – Rome	500

Table 0.2.1: Potential routes for a 500 km Hyperloop journey

To estimate Hyperloop energy demand, total consumption is divided into functional blocks: acceleration, cruise mode, braking, climate control, cooling, and an additional safety margin. This margin accounts for both energy losses and the limitations of real storage system efficiency.

It is important to note that for both the high-power charger and inductive charging systems, all subsystem energy will be supplied by a battery. In contrast, the hydrogen fuel cell system is designed as a hybrid solution — with an auxiliary battery and the fuel cell stack itself — for reasons that will be discussed later. Therefore, in this section, the term "battery" refers to the element responsible for covering the vehicle's total energy demand, regardless of the charging method adopted.

The following sections present the consumption of each functional block.

4.2.1 Acceleration Energy Calculation

Before calculating the energy consumption during acceleration, it is important to note that this study assumes a propulsion system fully integrated into the vehicle. In other words, no external infrastructure-mounted motor is considered to provide acceleration assistance. This approach allows for a complete energy analysis of the most demanding scenario, representing the case with the highest consumption required from the system.

An average acceleration of 1.1 m/s^2 —based on the Hardt proposal— has been selected for the energy calculations.

The time required to reach a velocity of 700 km/h —equivalent to 194.44 m/s— from standstill is approximately 3 minutes:

$$t\,(s) = \frac{V_{\text{final}}\left(\frac{m}{s}\right) - V_{\text{initial}}\left(\frac{m}{s}\right)}{a\left(\frac{m}{s^2}\right)} = \frac{194.44}{1.1} = 176.76\,s = 2'58''$$

Next, the power required during the acceleration phase is calculated using the following expression:

$$P\,(W) = F\,(N) \cdot V\,\left(\frac{m}{s}\right) = m\,(kg) \cdot a\,\left(\frac{m}{s^2}\right) \cdot v\,\left(\frac{m}{s}\right)$$

To perform this calculation, the total vehicle mass must be determined. The following table presents the mass breakdown by component:

Subsystem Breakdown	Weight (kg)
Payload - subtotal with cabin	43,000
Main body - subtotal	16,000
Tractive system - subtotal	40,000
Battery - subtotal	22,222
Cooling system	3,000
TOTAL	**124,222**

Table 0.2.2: Mass breakdown of the Hyperloop vehicle

For this mass estimation, given the limited information available on real prototypes, the design proposed by Hardt was used as a reference. In their 40-passenger model, the total load and structural mass is significantly lower, so in this study, that value was linearly scaled by a factor of five to match a 200-passenger configuration.

Regarding the traction, levitation, and guidance systems, while some components would benefit from economies of scale —since their mass does not increase strictly proportionally to power or payload— the total mass increase of the vehicle would also affect these systems. Based on this premise, an increase of three to four times over the original design could be expected. Here, a conservative factor of four has been applied.

The battery mass was initially estimated and later adjusted according to the energy density of the selected type until the final value shown in the table was obtained.

The mass of the climate control and cooling system was estimated at 3,000 kg, based on a thermal demand of approximately 250 kW and taking as reference equivalent commercial solutions [21]. The origin and justification of this thermal power will be detailed later in this study.

For the power calculation during acceleration, it is not representative to simply take the power required at maximum speed —700 km/h—, as energy consumption varies throughout this phase. Therefore, the 3-minute acceleration interval was divided into 50 km/h segments to better estimate the average power under realistic operating conditions.

The required power at various speeds is shown in the following table:

Time (s)	Speed (km/h)	Speed (m/s)	Power (kW)
0.0	0.0	0.0	0.0
12.9	50.0	13.9	1,708.1
25.7	100.0	27.8	3,416.1
38.6	150.0	41.7	5,124.2
51.4	200.0	55.6	6,832.2
64.3	250.0	69.4	8,540.3
77.1	300.0	83.3	10,248.3
90.0	350.0	97.2	11,956.4
102.9	400.0	111.1	13,664.4
115.7	450.0	125.0	15,372.5
128.6	500.0	138.9	17,080.5
141.4	550.0	152.8	18,788.6
154.3	600.0	166.7	20,496.6
167.1	650.0	180.6	22,204.7
180.0	700.0	194.4	23,912.7

Table 0.2.3: Required power at various speeds during acceleration

A Hyperloop vehicle with a capacity for 200 passengers must be capable of delivering a peak power close to 24 MW, with an average demand of about 12 MW during acceleration. This average power over 3 minutes results in an energy consumption of:

$$E\,(\text{kWh}) = P\,(\text{MW}) \cdot t\,(\text{h}) = 12 \cdot \frac{3}{60} = 12 \cdot 0.05 = 0.6\,\text{MWh} = 600\,\text{kWh}$$

Finally, the distance covered during acceleration is:

$$s\,(m) = v_i \left(\frac{m}{s}\right) \cdot t\,(s) + \frac{1}{2} \cdot a \left(\frac{m}{s^2}\right) \cdot t^2\,(s^2) = 0 \cdot 178 + 0.5 \cdot 1.1 \cdot 178^2 = 17{,}426\,\text{m} \approx 17.4\,\text{km}$$

4.2.2 Braking Energy Calculation

During the braking phase, a regenerative braking system is considered the primary deceleration strategy. This technology enables part of the vehicle's kinetic energy to be recovered and converted into electrical energy, which can be stored in the on-board batteries. In the case of Hyperloop, the linear motor-based traction system temporarily reverses during braking, so that the vehicle's inertia acts on the system and allows the motors to function as generators. This energy conversion takes

place through the on-board electromagnetic coils, eliminating the need for traditional mechanical elements such as wheels or friction brakes.

Moreover, this type of braking can be applied continuously through micro-braking, particularly useful on downhill sections or during speed regulation, helping to keep the battery partially charged throughout the trip.

Several studies have shown that this technology can achieve regeneration efficiencies above 90% under optimal conditions [11], although in practice it typically ranges between 75% and 85%. In this study, a conservative value of 80% regenerative efficiency is adopted for energy calculations associated with this phase.

The recovered energy is calculated as follows:

$$E_k\,(J) = \frac{1}{2}\,m\,(kg)\,v^2\,\left(\frac{m^2}{s^2}\right) = 0.5 \cdot 124{,}222 \cdot 194.44^2 = 2{,}362{,}706{,}250\,J$$

$$E_{\text{recovered}}\,(J) = E_k \cdot \eta = 2{,}362{,}706{,}250 \cdot 0.80 = 1{,}890{,}165{,}000\,J$$

Conversion to kWh:

$$E\,(kWh) = \frac{E\,(J)}{3.6 \times 10^6} = \frac{1{,}890{,}165{,}000}{3{,}600{,}000} = 525.05\,kWh \approx 525\,kWh$$

Thus, regenerative braking supplies approximately 525 kWh directly back to the battery.

Finally, deceleration occurs at a rate of 1.5 m/s², resulting in:

$$t\,(s) = \frac{V_{\text{final}}\,\left(\frac{m}{s}\right) - V_{\text{initial}}\,\left(\frac{m}{s}\right)}{a\,\left(\frac{m}{s^2}\right)} = \frac{194.44}{1.5} = 129.62\,s = 2'10''$$

And the distance covered during braking is:

$$s\,(m) = v_i\,\left(\frac{m}{s}\right)\cdot t\,(s) + \frac{1}{2}\cdot a\,\left(\frac{m}{s^2}\right)\cdot t^2\,(s^2) = 194.44\cdot 129.63 + 0.5\cdot(-1.5)\cdot 130^2 = 12{,}602\,m \approx 12.6\,km$$

4.2.3 Cruise Mode Energy Calculation

One of the key advantages of Hyperloop technology is the significant reduction of aerodynamic losses compared to conventional high-speed trains. This is because the vehicle travels inside a low-pressure tube, at around 1 millibar, which greatly reduces air resistance and enables high speeds with lower energy demand. However, as the system does not operate in a perfect vacuum, a residual amount of air still generates measurable aerodynamic drag.

It is also necessary to account for the energy required to sustain the magnetic fields of the levitation and guidance system. According to Hardt's study, for a train with a 40-passenger capacity, aerodynamic drag is approximately 1,450 N, and maintaining the electromagnetic fields requires about 1,650 N. When scaling to a 200-passenger vehicle, it is assumed the train is lengthened without increasing its frontal area, so aerodynamic losses remain constant. However, the energy associated with the magnetic fields increases by a factor of 4, as applied previously to the levitation and traction system mass.

The power required during cruise mode is calculated as:

$$P\,(W) = F\,(N) \cdot v\,\left(\frac{m}{s}\right) = (1{,}650 \cdot 4 + 1{,}450) \cdot 194.44 = 8{,}050 \cdot 194.44 = 1{,}565{,}222\,W \approx 1.565\,\text{MW}$$

The combined distance covered during acceleration and braking totals 30 km, leaving 470 km for cruise. At 700 km/h, this corresponds to 40.3 minutes of travel time. The energy consumed during cruise is:

$$E\,(kWh) = P\,(kW) \cdot t\,(h) = 1{,}565 \cdot \frac{40.3}{60} = 1{,}565 \cdot 0.6717 = 1{,}050\,\text{kWh}$$

Thus, cruise mode results in an energy demand of approximately 1,050 kWh.

4.2.4 Cooling & Climate Control Energy Calculation

The following section details the energy calculations related to auxiliary system consumption, with cooling and climate control as the main contributors. For this reason, these demands are grouped under the term cooling consumption.

The components of this block are broken down as follows:

- **Climate control —HVAC—**: includes heating, ventilation, and air conditioning systems, responsible for maintaining thermal comfort conditions. It is estimated that a person at rest emits between 60 and 100 W of body heat. In the most demanding case, with 200 passengers on board and assuming 100 W per passenger, this results in a thermal load of 20 kW.
- **Lighting**: covers both interior and exterior lighting, including emergency lighting. The estimated maximum consumption is 10 kW.
- **Automatic doors**: refers to the mechanisms for passenger access. The estimated required power is 5 kW.
- **Control and safety systems**: includes signaling, train control, surveillance, communication systems —displays, audio announcements, etc.—. The estimated combined consumption is 25 kW.
- **Propulsion cooling losses**: Assuming 90% traction efficiency, 10% of the average 12 MW used during acceleration is lost as heat —1,200 kW—. Of this, 10% is estimated to require removal by dedicated cooling systems, translating to an additional 120 kW.

- **Thermal insulation losses and parasitic gains**: In the most demanding case, these could account for up to 15 kW of losses.

It is worth noting that losses in the levitation systems have been neglected, as they mainly consist of permanent magnets that do not generate significant thermal losses during operation.

Finally, although the vehicle operates in a sealed environment isolated from external conditions, it is recommended to apply an oversizing margin of 20–30% to cooling and climate control systems to ensure proper performance in critical internal situations, such as heat accumulation during prolonged acceleration, energy demand peaks, or local failures in thermal dissipation.

Cooling System Breakdown	Power (kW)
HVAC	20
Lighting	10
Automatic Doors	5
Control and Safety Systems	25
Propulsion Cooling Losses	120
Thermal Insulation Losses	15
TOTAL	195
Security margin -30%-	253.5
TOTAL CONSUMPTION (kWh)	204

Table 0.2.4: Cooling system power consumption breakdown

The total consumption is 204 kWh over the entire trip duration of 45 minutes and 28 seconds.

4.2.5 Total Energy Consumption Calculation

After analyzing the different energy demands corresponding to each phase of the journey, the total required energy is calculated. This requires accounting for the efficiency of the storage system. The selected battery —whose choice is justified in the following section— is based on LTO technology and has an efficiency of 90%.

In addition, following the same criterion applied to the cooling system, a 30% oversizing margin has been included. This decision is justified by the fact that the journey involves no intermediate stops, where any interruption in energy supply could be critical. It is also important to note that the energy recovered through regenerative braking is only available at the end of the journey, which reinforces the need to ensure sufficient energy availability throughout the entire operation.

The total energy consumption is expressed as:

$$E_{\text{total}}\,(\text{kWh}) = \frac{E_{\text{acceleration}} + E_{\text{cruise}} + E_{\text{cooling}} - E_{\text{brake}}}{\eta} \cdot 1.3 = \frac{600 + 1{,}050 + 204 - 525}{0.9} \cdot 1.3 = 1{,}920\,\text{kWh} \approx 2\,\text{M}$$

Since the energy recovered from regenerative braking is only available at the end of the trip, the final result has been rounded to a total capacity of 2 MWh, ensuring a sufficient energy margin for the entire operation.

4.2.6 Battery Selection Rationale and Supercapacitor Assessment

When determining whether acceleration should be powered by a battery or by supercapacitors, the two key parameters considered were the maximum discharge rate and the energy density. Given that during the acceleration phase the vehicle requires a peak power of 24 MW and the battery capacity is sized at approximately 2 MWh, the necessary discharge rate is around 12 C.

After analyzing different commercial storage technologies, a Lithium Titanate Oxide —LTO— battery was selected due to its excellent power performance. These batteries allow continuous discharge rates of up to 10 C and can reach up to 20 C for short pulses (under one minute), making them particularly suitable for covering the peak power demands during Hyperloop acceleration.

However, compared to other options such as Lithium Iron Phosphate —LFP— batteries, LTO batteries have a lower energy density —90 Wh/kg—, which results in greater volume and mass for the same storage capacity. Additionally, the cost per kWh is significantly higher, which could impact the overall system budget [7, 19].

The following table shows the maximum discharge rates required during the acceleration profile, as a function of the speed reached and the power demanded in each segment:

Max Discharge Rate (C)	Time (s)	Speed (km/h)	Speed (m/s)	Power (kW)
0.0	0.0	0.0	0.0	0.0
0.9	12.9	50.0	13.9	1708.1
1.7	25.7	100.0	27.8	3416.1
2.6	38.6	150.0	41.7	5124.2
3.4	51.4	200.0	55.6	6832.2
4.3	64.3	250.0	69.4	8540.3
5.1	77.1	300.0	83.3	10248.3
6.0	90.0	350.0	97.2	11956.4
6.8	102.9	400.0	111.1	13664.4
7.7	115.7	450.0	125.0	15372.5
8.5	128.6	500.0	138.9	17080.5
9.4	141.4	550.0	152.8	18788.6
10.2	154.3	600.0	166.7	20496.6
11.1	167.1	650.0	180.6	22204.7
12.0	180.0	700.0	194.4	23912.7

Table 0.2.5: Maximum discharge rate required during the acceleration profile

As observed, the 10 C threshold is exceeded for approximately 26 seconds in this study. Therefore, the battery system must be equipped with enhanced cooling to ensure stable operation throughout the acceleration profile. It is important to highlight that this extreme demand only occurs for a very short duration, minimizing the risk of premature degradation if the system is properly thermally managed.

Thanks to the properties of LTO batteries, their ability to operate at high charge and discharge rates, even in transient regimes, makes them an ideal candidate for a real Hyperloop system.

However, this study does not address the detailed design of the battery topology —that is, the number of series/parallel cells or the battery management system —BMS— as the aim is to analyze and compare different power supply systems. Likewise, the specific analysis of the propulsion subsystem, its technical characteristics, and electrical requirements is beyond the scope of this study.

In parallel, the possibility of using supercapacitors to provide the peak energy required for acceleration was also examined. Although supercapacitors offer extremely high power density, their low energy density —10 Wh/kg— limits their application in systems like Hyperloop, where no recharging opportunity exists during the trip. Since all energy must be available from the start, the decisive factor in sizing their mass is the energy they can store, not the rate at which they deliver it.

The table below compares the mass of supercapacitors and batteries. In the first case, supercapacitors cover the entire power required during acceleration. In the other two scenarios, they serve as support during the final acceleration segments, reducing the discharge demand on the main battery:

What supercaps covers	Weight supercaps (kg)	Weight battery (kg)
All the acceleration	59781.8	11700.0
From 500–700 km/h	29280.9	16105.7
From 600–700 km/h	15860.5	18161.7

Table 0.2.6: Comparison of mass for supercapacitors and batteries in various scenarios

As seen, when supercapacitors are used to cover the entire acceleration phase, the total system mass increases considerably due to their low energy density. However, when limited to supporting only the most demanding segments —e.g., 500–700 km/h or 600–700 km/h—, the additional mass is reduced significantly, achieving a better balance between performance and total mass.

Nonetheless, compared to the option of using only a battery, the inclusion of supercapacitors represents substantial additional weight, which could otherwise be avoided.

4.3 Hydrogen Fuel Cells

In this section, the use of hydrogen fuel cell systems is considered as a potential power source for a real Hyperloop vehicle.

In the context of sustainable energy solutions for high-speed transport systems like Hyperloop, hydrogen fuel cells emerge as a promising technology for clean, efficient, and modular power generation. Compared to traditional sources such as grid connection or the exclusive use of electric batteries, fuel cells offer significant energy autonomy with no direct emissions of polluting gases, enhancing both environmental sustainability and operational viability, particularly on long routes or in isolated infrastructures.

This power system is designed to meet an energy demand of 2 MWh, as previously defined. For this purpose, Proton Exchange Membrane —PEM— fuel cells are considered, supplied by high-pressure hydrogen and pure oxygen instead of ambient air. This choice maximizes the energy efficiency of the electrochemical reaction, simplifies the gas purification system, and reduces the required intake volume, which is particularly important in confined environments where gases cannot be vented, such as inside the Hyperloop tube. Consequently, the entire system must be designed to store all the hydrogen and oxygen required for the reaction, as well as the water produced as a by-product.

At the infrastructure level, the need for pressurized tanks for hydrogen, oxygen, and the resulting water has been evaluated, all housed within the vehicle. The design explores several scenarios where an integrated mass and energy balance ensures the system's autonomy and safety, always supported by a battery to ensure proper startup and auxiliary system operation. For all proposed scenarios,

these tanks have been dimensioned, detailing their weight and volume. Additionally, an economic study has been conducted, analyzing both infrastructure costs and operational costs —hydrogen and oxygen supply—. Finally, these results have been compared to the alternative of relying solely on a battery system.

Lastly, aspects such as the technological maturity of this solution, its operational safety, service life, modularity, refueling time, and scalability have been discussed to compare it against the other power supply systems.

4.3.1 Hydrogen Fuel Cell Operation

First, a PEM fuel cell consists of three fundamental elements:

- **Anode**: positive electrode.
- **Cathode**: negative electrode.
- **Electrolyte membrane**.

Hydrogen —H_2— is introduced through channels machined into the anode-side plate, passes through a carbon-based diffusion layer, and reaches the catalytic layer, where the hydrogen oxidation reaction takes place:

$$\text{Anode reaction: } H_2 \rightarrow 2H^+ + 2e^-$$

The protons generated pass through the polymer membrane, while the electrons are forced to travel through an external circuit, as the membrane is electrically insulating. This electron flow generates the electric current required to perform work.

At the cathode, oxygen from the tank diffuses through its diffusion layer to the catalytic layer. Here, it reacts with the protons and electrons from the external circuit to form water:

$$\text{Cathode reaction: } \frac{1}{2}O_2 + 2H^+ + 2e^- \rightarrow H_2O + Q$$

Finally, the overall reaction is:

$$\text{Overall reaction: } H_2 + \frac{1}{2}O_2 \rightarrow H_2O + Q$$

As by-products, heat and water are generated, which are expelled at the cathode. The additional heat is dissipated by forced convection through a closed-loop cooling system consisting of a heat exchanger that uses glycol with low electrical conductivity as the coolant. This coolant is advantageous as it poses no corrosion risk to the components. It is worth noting that the design of the cooling and heat dissipation system of the fuel cells is beyond the scope of this study.

The term “fuel cell” refers to the assembly of multiple single cells, where the electrons proceed to the cathode of the adjacent cell instead of returning to the same cell’s cathode, a process known as cascading. This enables higher voltage and power generation, essential for real applications such as meeting the demands of a Hyperloop vehicle.

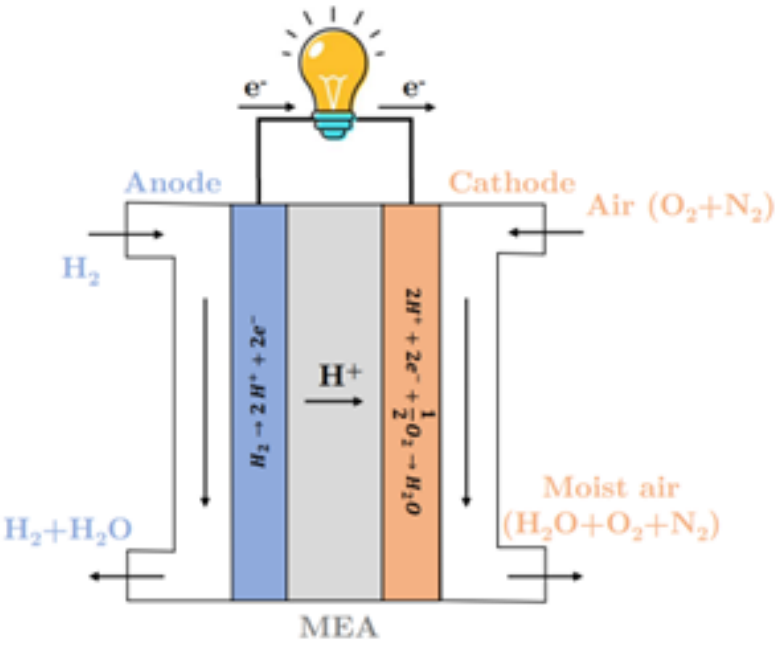

Figure 0.3.1: Operation of a PEM hydrogen fuel cell. Source: López (2022) [15].

4.3.2 Definition and Justification of Operating Scenarios

First, it is necessary to establish some key considerations. Hydrogen fuel cells for mobile applications have an efficiency of about 50% [15], which is significantly lower compared to other power supply systems. Furthermore, the reaction temperature of these fuel cells is approximately 70 ºC [**?**], meaning the water produced will be in liquid form.

As previously discussed in Section 4.2.5, the total energy demand to be covered by the vehicle is 2 MWh, distributed as follows: acceleration —24 MW peak, 12 MW average, 600 kWh—, cruise —1.565 MW, 1050 kWh—, cooling and climate control —204 kWh—, safety margin —671 kWh—, and regenerative braking —- -525 kWh, negative due to energy recovery—. In applications such as a Hyperloop vehicle, this technology is configured as a hybrid system, combining fuel cells with a battery. To utilize regenerative braking, at minimum a battery capable of storing the recovered energy —525 kWh— is required. Additionally, hydrogen fuel cells cannot operate without a support battery, as energy is needed for startup and for auxiliary systems in case of fuel cell failure.

It is crucial to understand that hydrogen fuel cells must be designed so that their installed power matches the maximum required power. In the case of acceleration, even if the average power is 12 MW, the system must be capable of delivering 24 MW continuously. Otherwise, achieving the peak power would be impossible.

Based on this, four scenarios are proposed where the maximum installed hydrogen power on board varies. The maximum deliverable power is used to assess the economic cost, weight, and occupied volume of each scenario. Meanwhile, for hydrogen, oxygen, and water consumption and production, the average acceleration power is used.

The following two tables show in detail the energy produced by the hydrogen fuel cell system in each scenario, as well as the battery energy consumption. The useful power that hydrogen must supply during the acceleration and cruise phases is also presented.

H2 ENERGY PROD. (kWh)	Acceleration	Cruise	Refrigeration	Security margin	TOTAL	AVG POWER ACCEL. (kW)	AVG POWER CRUISER (kW)
H2 24 MW	600	1050	204	146	2000	12000	2027
H2 18 MW	450	1050	204	500	2204	9000	2225
H2 12 MW	300	1050	-	175	1525	6000	1795
H2 6 MW	150	-	204	671	1025	3000	1154

Table 0.3.1: Energy produced by hydrogen fuel cell system in each scenario

BATTERY ENERGY PROD. (kWh)	Acceleration	Cruise	Refrigeration	Security margin	TOTAL	END OF TRIP ENERGY	BATTERY CAPACITY (kWh)
H2 24 MW	0	-	-	525	525	525	525
H2 18 MW	150	-	-	375	525	525	525
H2 12 MW	300	-	204	496	1000	525	1000
H2 6 MW	450	1050	-	-	1500	525	1500

Table 0.3.2: Battery energy production and capacity in each scenario

According to the formulas presented in the following sections, to calculate hydrogen and oxygen consumption, as well as water production, it is necessary to know the net power required for each phase. For these calculations, the demand is divided between the acceleration and cruise phases. The energy consumed for cooling and the safety margin, in the worst case —where all of it is used—, is converted into power based on the total journey duration. This power is then added to the required cruise power. As a result, in all four scenarios, although only 1525 kW is needed for cruise, the average power during this phase is higher.

A brief explanation of each scenario is provided below:

- **Scenario 1**: The hydrogen fuel cells are designed to cover the energy demand of the entire acceleration phase, cruise, cooling, and part of the safety margin. During acceleration, the system would provide the 24 MW peak power required, and during cruise, it would continuously deliver 2,027 kW of power.
    - The battery, with a capacity of 525 kWh, would cover most of the safety margin allocation, remaining fully charged at the end of each journey.
- **Scenario 2**: The hydrogen fuel cells are designed to cover most of the acceleration demand, cruise, cooling, and part of the safety margin. The power during acceleration is shared between the hydrogen fuel cell system and the battery. The fuel cells provide 18 MW peak —9 MW average—, and the battery supplies the remaining 6 MW peak.
    - The battery, with a capacity of 525 kWh, covers part of the safety margin and part of the acceleration, remaining fully charged at the end of each trip.
    - Compared to Scenario 1, this approach reduces installed power, lowering weight and cost —as will be shown later—. However, the required cruise power is slightly higher —2,225 kW.

- **Scenario 3**: The hydrogen fuel cells are designed to cover half of the acceleration demand, cruise, and part of the safety margin. With 12 MW of installed power, the battery must provide the other half of the peak power during acceleration.
    - The battery has a large capacity of 1 MWh, due to the maximum discharge rate requirements —explained below—. It covers half of the acceleration power, as well as cooling and most of the safety margin.
    - The hydrogen system, although capable of providing 12 MW continuously, requires only 1,795 kW on average during the remainder of the journey.
- **Scenario 4:** The hydrogen fuel cells, with a power of 6 MW, cover only a quarter of the acceleration demand, cooling, and the safety margin.
    - The battery, again driven by the discharge rate criterion, has a capacity of 1.5 MWh. It fully covers the cruise power demand and most of the acceleration.
    - The hydrogen system provides only 1,154 kW continuously to meet the cooling and safety margin needs, well below its maximum capacity.

It is important to highlight that for the selection of scenarios, the battery's discharge rate during acceleration and maximizing its energy use —to avoid oversizing— have been key criteria. As discussed in 4.2.6, if only a battery were used as the energy source for the vehicle, it could not exceed a discharge rate of 12 C, which already pushes its limits. Therefore, Scenarios 3 and 4 feature larger batteries compared to the first two. The reduction in installed hydrogen power necessitates increasing battery capacity to meet this criterion.

The following table shows the battery's maximum discharge rate in each scenario:

Scenario	Max Discharge Rate (C)
1) H2 24 MW	-
2) H2 18 MW	11.43
3) H2 12 MW	12
4) H2 6 MW	12

Table 0.3.3: Maximum battery discharge rate in each scenario

In the first case, since all the required acceleration power is provided by hydrogen, the battery's maximum discharge rate is not critical.

Regarding the distribution between energy supplied by the battery and by the fuel cells, there is a clear imbalance between the installed hydrogen power and its utilization during cruise. A very high hydrogen power is installed to handle acceleration, but much of this capacity goes unused during the rest of the trip. This is because a large battery capacity is mandatory, as explained earlier. Using hydrogen and oxygen to generate energy instead of relying on the available battery charge would unnecessarily increase the size and cost of the pressurized tanks.

Finally, it can be verified that the total energy provided by both systems in each scenario amounts to 2,525 kWh. Subtracting the 525 kWh recovered through regenerative braking results in the initial assumed energy demand —2 MWh— in all cases. Furthermore, as the battery's energy has been maximally utilized, it retains at least 525 kWh at the end of each trip —in case less cooling or safety margin energy was consumed—.

4.3.3 Consumption and Production Calculation

The next step is to calculate, for each case, the minimum required consumption of H_2 and pure O_2 per trip, as well as the amount of water produced in the reaction.

Due to the characteristics of the Hyperloop environment—operating in a near-vacuum—it is not possible to release heat or gases to the outside. Therefore, the system must be designed to store both the reactants and the products of the reactions inside the vehicle until they can be replenished or removed. To store the hydrogen and oxygen, pressurized tanks are required at 700 bar and 200 bar respectively, the maximum commercial storage pressure typically used for these gases. A water tank is also needed to contain the reaction product. Storing these reactants inside a vacuum tube at millibar pressures adds significant complexity to the safety design.

Before starting the actual calculations, the operating conditions are defined as follows:

- **System efficiency:** 50%
- **Fuel cell operating temperature:** 70 °C or 343.15 K
- **Reactant storage temperature:** 25 °C or 298.15 K
- **Fuel cell operating pressure:** 1.013 bar
- **H_2 tank pressure:** 700 bar
- **O_2 tank pressure:** 200 bar
- **Stoichiometry at cathode and anode:** 1 —minimum consumption estimated without excess reactants—
- **Ideal gas constant:** $R = 8.314$ J/mol·K
- **Molar masses:**
  - **H_2O:** 18 g/mol
  - **H_2:** 2.01568 g/mol
  - **O_2:** 32 g/mol
- **H_2 compressibility factor at 700 bar and 25°C:** $Z = 1.44991$ [6]
- **O_2 compressibility factor at 200 bar and 25°C:** $Z = 1$ [24]
- **Lower heating value of H_2:** 33.33 kWh/kg H_2

The following describes how to calculate the quantities of reactants consumed and products obtained:

The hydrogen consumption —kg/h— is calculated using:

$$\dot{m}_{\mathrm{H_2}}\,(\mathrm{kg/h}) = \frac{\mathrm{Power}\ (\mathrm{kW})}{\eta \cdot \mathrm{LHV}_{\mathrm{H_2}}\ (\mathrm{kWh/kg})}$$

The oxygen consumption —kg/h— is calculated using the stoichiometric mass balance derived from the molar balance of the reaction:

$$\dot{m}_{\mathrm{O_2}}\,(\mathrm{kg/h}) = \dot{m}_{\mathrm{H_2}}\,(\mathrm{kg/h})\frac{\mathrm{M}_{\mathrm{H_2}}\ (\mathrm{g/mol})}{1} \cdot 0.5 \cdot \frac{\mathrm{M}_{\mathrm{O_2}}\ (\mathrm{g/mol})}{1}$$

Water production —kg/h— is calculated as:

$$\dot{m}_{\mathrm{H_2O}}\,(\mathrm{kg/h}) = \dot{m}_{\mathrm{H_2}}\,(\mathrm{kg/h})\frac{\mathrm{M}_{\mathrm{H_2}}\ (\mathrm{g/mol})}{1} \cdot \frac{\mathrm{M}_{\mathrm{H_2O}}\ (\mathrm{g/mol})}{1}$$

Since pure oxygen from a tank is used instead of air — and to minimize space and weight — the selected fuel cell does not require a humidifier. Furthermore, the specific fuel cell model and any potential need for a humidifier — to maintain ionic conductivity — are beyond the scope of this study.

As noted earlier, the water produced in the reaction is assumed to be entirely in liquid state since the operating temperature is below evaporation point — 70 °C.

To calculate the total mass of H_2, O_2 and H_2O, the mass flow rate in kg/h is multiplied by the corresponding operating time — 3 minutes for acceleration and 40.3 minutes for cruise. The deceleration phase is omitted since the hydrogen fuel cells provide no propulsion power during this stage — their contribution is negligible compared to the other phases. During deceleration, the battery supplies power for cooling, climate control, and safety margin — potentially using energy recovered through regenerative braking for these functions.

For volume calculation, the ideal gas equation corrected with the compressibility factor is used:

$$P\,(\mathrm{Pa}) \cdot V\,(\mathrm{m^3}) = Z \cdot n\,(\mathrm{mol}) \cdot R\,(\mathrm{J/mol \cdot K}) \cdot T\,(\mathrm{K})$$

After rearranging, it can be expressed in its final form for use:

$$V\,(\mathrm{L}) = Z \cdot m\,(\mathrm{kg}) \cdot R\,(\mathrm{J/mol \cdot K}) \cdot T\,(\mathrm{K}) / \left(\mathrm{M}\,(\mathrm{kg/mol}) \cdot P\,(\mathrm{Pa})\right) \cdot 1000$$

Water volume is assumed equal to its mass — 1 kg H_2O equals 1 L H_2O.

This provides the mass and volume of reactants and products — essential for operational cost estimation and tank design.

4.3.3.1 Consumption and Production Results

Starting with the first case, the following tables show the mass flows during both acceleration and cruise phases, along with the respective masses and volumes:

Species consumption and production	Flow (kg/h)	Mass (kg)	Volume (L)
Hydrogen consumption	720.07	36.00	917.09
Air / Oxygen consumption	5715.76	285.79	1604.91
Water production	6430.24	321.51	321.51

Table 0.3.4: CASE 1 (24 MW PEAK - 12 MW AVG): Acceleration Consumption and Production (3 min)

Species consumption and production	Flow (kg/h)	Mass (kg)	Volume (L)
Hydrogen consumption	121.63	83.12	2117.13
Air / Oxygen consumption	965.49	659.75	3704.98
Liquid water	1086.17	742.22	742.22

Table 0.3.5: CASE 1 —1.85 MW—: Cruiser & Refrigeration Consumption and Production —42 min 28 sec—

The consumption during acceleration and cruise for the second configuration is presented below:

Species consumption and production	Flow (kg/h)	Mass (kg)	Volume (L)
Hydrogen consumption	540.05	27.00	687.82
Air / Oxygen consumption	4286.82	214.34	1203.68
Water production	4822.68	241.13	241.13

Table 0.3.6: CASE 2 —18 MW PEAK — 9 MW AVG): Acceleration Consumption and Production —3 min—

Species consumption and production	Flow (kg/h)	Mass (kg)	Volume (L)
Hydrogen consumption	133.51	92.35	2352.27
Air / Oxygen consumption	1059.80	733.03	4116.48
Liquid water	1192.27	824.66	824.66

Table 0.3.7: CASE 2 —2.225 MW—: Cruiser, Refrigeration & Margin Consumption and Production —42 min 28 sec—

Starting with the first case, the following tables show the mass flows during both acceleration and cruise phases, along with the respective masses and volumes:

Table 0.3.8: Case 3 —12 MW Peak - 6 MW Avg—: Acceleration Consumption and Production —3 min—

Species consumption and production	Mass flow (kg/h)	Mass (kg)	Volume (L)
Hydrogen consumption	360.04	18.00	458.55
Air / Oxygen consumption	2857.88	142.89	802.45
Water production	3215.12	160.76	160.76

Table 0.3.9: Case 3 —1.795 MW—: Cruiser & Part Margin Consumption and Production —42 min 28 sec—

Species consumption and production	Mass flow (kg/h)	Mass (kg)	Volume (L)
Hydrogen consumption	107.71	72.35	1842.80
Air / Oxygen consumption	854.98	574.26	3224.91
Liquid water	961.86	646.05	646.05

Finally, the consumption data for the fourth configuration:

Table 0.3.10: Case 4 —6 MW Peak - 3 MW Avg—: Acceleration Consumption and Production —3 min—

Species consumption and production	Mass flow (kg/h)	Mass (kg)	Volume (L)
Hydrogen consumption	180.02	9.00	229.27
Air / Oxygen consumption	1428.94	71.45	401.23
Water production	1607.56	80.38	80.38

Table 0.3.11: Case 4 —1.154 MW—: Cruiser & Part Margin Consumption and Production —42 min 28 sec—

Species consumption and production	Mass flow (kg/h)	Mass (kg)	Volume (L)
Hydrogen consumption	69.25	49.05	1249.41
Air / Oxygen consumption	549.67	389.35	2186.46
Liquid water	618.37	438.02	438.02

The comparison of consumption and production across all cases is summarized in the following table:

Table 0.3.12: Overall comparison of species consumption and production across scenarios

Overall Comparison	1: H2 24 MW		2: H2 18 MW		3: H2 12 MW		4: H2 6 MW	
Species consumption and production	Mass (kg)	Volume (L)	Mass (kg)	Volume (L)	Mass (kg)	Volume (L)	Mass (kg)	Volume (L)
Hydrogen consumption	119.12	3034.22	119.35	3040.09	90.35	2301.35	58.05	1478.68
Oxygen consumption	945.54	5309.88	947.37	5320.16	717.16	4027.36	460.79	2587.69
Liquid water	1063.73	1063.73	1065.79	1065.79	806.80	806.80	518.39	518.39

As shown in the comparative table, Cases 1 and 2 present very similar hydrogen and oxygen consumption levels despite the difference in installed peak power. This is because, in Case 2, although the maximum power of the hydrogen fuel cells is lower, the increased demand during cruise compensates for the initial reduction.

Case 3 shows a reduction in total consumption compared to the first two cases, falling between those and the fourth configuration. Despite the notable reduction in installed power, the required power during cruise remains high — 1,795 kW — causing the results to be closer to the first two cases than to the last one.

It is in the fourth case where the lowest hydrogen and oxygen consumption is achieved, as it is designed to deliver a maximum of 6 MW during acceleration and 1,154 kW during cruise. Although this is the most energy-efficient option, the reduction in hydrogen power comes with greater reliance on the battery, resulting in increased size and capacity, as also observed in Case 3.

These results have enabled precise sizing of the storage tanks for each configuration and provide the foundation for subsequent analysis of weights, volumes, and total costs associated with each energy setup.

4.3.3.2 Operational Cost Calculation

Before proceeding with the cost analysis, it is essential to note that for this study both H and O are stored in compressed gaseous form. For the calculation of operational costs, a comprehensive market study was conducted, considering the pressures at which each compound is stored and analyzing the various prices offered by manufacturers and distributors capable of supplying gas under the conditions required by this study — that is, H stored at 700 bar and O at 200 bar.

Once the quantities of oxygen, hydrogen, and water required per trip had been determined, the respective costs were calculated. In the case of a Hyperloop vehicle with a journey duration of approximately 48 minutes, it is assumed that it would complete a minimum of six trips per day, resulting in approximately 2,200 trips per year. For this reason, operational costs are compared both on a per-trip basis and for a total of 2,200 trips. Furthermore, the results are compared with the equivalent cost of using a battery system capable of supplying the 2 MWh of energy demand required.

First, in order to calculate the operational cost of hydrogen, it is necessary to establish the cost per kilogram of H. Based on the market study conducted, the following table presents the various prices

offered by hydrogen distribution stations across Europe [2], from which an average price was derived:

Table 0.3.13: Hydrogen price by country

Country	Hydrogen Price (€/kg H2)
Netherlands	17.50
Netherlands	20.29
Netherlands	21.95
Germany	16.50
Germany	18.25
Germany	18.25
France	18.66
Belgium	9.99
Average	**17.67**

It should be emphasized that the hydrogen used in this technology must have a minimum purity of 99.99999 percent. Pure hydrogen is produced through processes such as methane reforming, water electrolysis, gasification, and other emerging technologies. At present, the majority of hydrogen produced on an industrial scale originates from fossil sources. However, the medium-term objective is to transition toward green hydrogen, generated through electrolysis powered by renewable energy sources, thereby enabling clean and sustainable production without CO emissions.

Regarding its price, hydrogen costs vary between countries, influenced to a significant extent by the level of available subsidies. The previous table presents an average of current prices, though it is anticipated that these will decrease over time as the technology matures and the cost of producing green hydrogen becomes more competitive. For the specific case of calculating the operational cost of pure H used to power a Hyperloop vehicle, it is sufficient to multiply the average price per kilogram of hydrogen by the H consumption figures calculated for each case.

Similarly, for the calculation of the cost associated with oxygen consumption, a market study was also conducted [1]. A commercial 50-liter O cylinder pressurized at 200 bar is capable of storing up to 10,000 liters, according to Boyle-Mariotte's law:

$$V_2\,(\mathrm{L}) = \frac{p_1\,(\mathrm{bar})}{p_2\,(\mathrm{bar})} \cdot V_1\,(\mathrm{L}) = \frac{200}{1} \cdot 50 = 10{,}000\,\mathrm{L}$$

After a review of various manufacturers, the oxygen content in these cylinders is valued at approximately 140 euros, resulting in a unit cost of 0.014 euros per liter of O. Once the volume of O consumed has been determined, the corresponding operational cost per trip can be calculated.

Furthermore, since all configurations require the inclusion of a battery, the cost of electricity has been considered within this study. Taking as a reference the average electricity price recorded in

Spain during March — according to OMIE, the Iberian Electricity Market Operator — the value stands at 55.52 euros per MWh, equivalent to 0.05552 euros per kWh [3].

In the first and second configurations — where the battery capacity amounts to 525 kWh — it is assumed that the battery is fully recharged at the end of each trip by means of regenerative braking, thus incurring no operational cost. The electricity cost is only accounted for in the third and fourth configurations, as well as in the fully electric alternative referred to as Case 5. In Cases 3 and 4, the energy recovered through regenerative braking is deducted from the total battery capacity required.

The comparative table of operational costs is presented below:

Operational Cost	H2 (€)	O2 (€)	Battery (€)	Total Cost Per Trip (€)	Total Cost 2200 Trips (€)
1: H2 24 MW	2104.83	74.34	0.00	2179.17	4,794,173.0
2: H2 18 MW	2108.90	74.48	0.00	2183.39	4,803,450.9
3: H2 12 MW	1596.44	56.38	26.37	1679.20	3,694,231.2
4: H2 6 MW	1025.76	36.23	54.13	1116.12	2,455,458.3
5: Only Battery	-	-	111.00	111.00	244,288.0

Table 0.3.14: Operational cost comparison for different power supply configurations.

The results reveal substantial differences in operational expenditure across the various configurations analyzed. The first four configurations — those incorporating hydrogen as the primary energy source — exhibit per-trip costs markedly higher than the fully battery-electric solution. This discrepancy becomes particularly evident when extrapolated to an annual scale of 2,200 trips, where hydrogen-based systems result in costs ranging from 2.6 to 4.8 million euros, compared to 244,288 euros for the fully electric configuration.

In the first configuration — featuring 24 MW of installed hydrogen power — one of the highest per-trip operational costs is recorded, amounting to 2,179.17 euros, primarily driven by elevated H and O consumption. The second configuration — with 18 MW of installed power — yields a comparable cost level, indicating that the reduction in installed fuel cell capacity does not yet translate into meaningful savings when the cruise power demand remains substantial.

The third case — with 12 MW of fuel cell power and increased reliance on battery storage — demonstrates a discernible reduction in operational cost per trip, reaching 1,679.20 euros. The fourth configuration — with 6 MW of installed fuel cell power — achieves the lowest operational cost among the hybrid alternatives at 1,116.12 euros per trip, albeit with a notable increase in battery-related costs.

A clear trend emerges from this analysis: the operational cost decreases progressively as hydrogen fuel cell usage is reduced. This constitutes a pivotal finding, underscoring the disproportionately high cost associated with hydrogen technology when compared to a strategy based on larger battery capacity.

It is crucial to highlight that these power supply architectures are designed for a train capable of accommodating up to 200 passengers — an operational expenditure of this magnitude would likely necessitate higher ticket pricing relative to the fully electric configuration.

4.3.4 Calculation of Weights, Volumes and Associated Infrastructure Costs

Before proceeding with the calculations, it is necessary to define the key concept of associated infrastructure analysis. This refers to the various additional elements that a Hyperloop vehicle would require internally in the event of employing hydrogen fuel cell technology. These elements include pressurized hydrogen tanks, pressurized oxygen tanks, a water tank, and the hydrogen fuel cells themselves. The different capacities and sizes of the battery in each configuration are also considered in order to carry out a broader and more realistic analysis.

This study excludes specific cooling systems that may be required, as well as power electronics and cabling, since these components are common across the different power supply systems analyzed.

4.3.4.1 Explanation of the Values Used

Starting with the hydrogen tank pressurized at 700 bar, two key concepts must be introduced —gravimetric capacity and volumetric capacity—. Gravimetric capacity refers to the percentage of hydrogen mass stored relative to the total system mass —H_2 plus tank— and indicates how lightweight the storage system is per unit of hydrogen. Volumetric capacity represents the amount of hydrogen stored per unit of system volume —g H_2 per L of tank—, indicating how compact the storage is.

The selected tank type corresponds to a Type IV hydrogen tank. To determine its gravimetric capacity, various Type IV H_2 tank manufacturers at 700 bar were analyzed, and an average value of 5% H_2 mass per system mass was established [20]. For volumetric capacity, according to the United States Department of Energy —DOE— [22], this value is 25 g H_2 per L of system volume. The average cost of an H_2 storage system of these characteristics is reported by the DOE at 15.7 dollars per kWh.

Regarding the oxygen tank, the most cost-effective solution identified is to store it in 50 L refillable cylinders — this being their physical volume — capable of holding up to 10,000 liters of gaseous O_2. The average empty weight of these cylinders is 72.4 kg, with a price of approximately 719 euros. As shown in the previous section, the volume of oxygen consumed in any scenario does not exceed 10,000 liters, so a single cylinder would suffice for the entire trip in all cases [16].

Moving on to the hydrogen fuel cell system, the concepts relating power output to its weight and volume are power density and volumetric power density, respectively. According to the DOE [23], the 2025 targets specify a power density of 650 W per kg, a volumetric power density of 650 W per L, and an estimated cost of 40 dollars per net kW. These values include the fuel cells themselves as well as the thermal management system and the balance of plant —BoP—. The balance of plant encompasses the auxiliary systems required for operation — including the oxygen supply system to the cathode, the hydrogen supply system to the anode, and the thermal management system that regulates stack temperature. These subsystems ensure that the fuel cell operates efficiently, safely, and stably.

It is clear that the first configuration will be particularly disadvantaged economically, as it must be designed to deliver 24 MW of peak power.

Lastly, for the calculation of battery weight and volume, both gravimetric and volumetric energy density values are required. The LTO —lithium-titanate oxide— battery — described previously — has an average gravimetric energy density of 90 Wh per kg and a volumetric energy density of 100

Wh per L. Due to technological advances, the current price of LTO batteries is around 139 dollars per kWh [8].

The key values used for calculating the weight, volume, and cost of the infrastructure associated with this technology are summarized below.

Hydrogen tank —H_2— Type IV, 700 bar

- Gravimetric capacity: 5 percent → 50 g H_2 per kg system
- Volumetric capacity: 25 g H_2 per L system
- Average cost: 15.7 dollars per kWh

Oxygen tank —O_2— Refillable cylinder

- Physical volume: 50 L
- Usable gaseous O_2 volume: up to 10,000 L
- Empty weight: 72.4 kg
- Approximate cost: 719 euros

Hydrogen fuel cell system

- Power density: 650 W per kg
- Volumetric power density: 650 W per L
- Estimated cost: 40 dollars per net kW
- Included components: fuel cell stack, thermal management system, balance of plant —BoP—

LTO battery —lithium-titanate oxide—

- Gravimetric energy density: 90 Wh per kg
- Volumetric energy density: 100 Wh per L
- Price: 139 dollars per kWh

4.3.4.2 Results of Weight, Volume and Associated Costs

First, the following table presents a comparison of the total weight of the different configurations:

INFRAESTRUCTURE WEIGHT	H2 TANK	O2 TANK	H2O TANK	FUEL CELL SYSTEM	BATTERY	TOTAL
1: H2 24 MW	2382.38	36.27	45.00	36923.08	5833.33	45220.06
2: H2 18 MW	2386.99	36.34	45.00	27692.31	5833.33	35993.97
3: H2 12 MW	1806.95	27.51	45.00	18461.54	11111.11	31452.11
4: H2 6 MW	1161.02	17.67	45.00	9230.77	16666.67	27121.13
5: ONLY BATTERY	-	-	-	-	22222.2	22222.2

Table 0.3.15: Total infrastructure weight for each configuration.

Regarding the volume occupied within the vehicle, the following table summarizes the conclusions:

INFRAESTRUCTURE VOLUME	H2 TANK	O2 TANK	H2O TANK	FUEL CELL SYSTEM	BATTERY	TOTAL	TOTAL (m^3)
1: H2 24 MW	4764.76	50.00	2000.00	36923.08	5250.00	48987.83	48.99
2: H2 18 MW	4773.98	50.00	2000.00	27692.31	5250.00	39766.29	39.77
3: H2 12 MW	3613.90	50.00	2000.00	18461.54	10000.00	34125.44	34.13
4: H2 6 MW	2322.03	50.00	2000.00	9230.77	15000.00	28602.80	28.60
5: ONLY BATTERY	-	-	-	-	20000.0	20000.0	20.00

Table 0.3.16: Total infrastructure volume for each configuration.

Finally, the following table presents the various manufacturing costs associated with the additional components required by this technology:

INFRAESTRUCTURE COST	H2 TANK (€)	O2 TANK (€)	H2O TANK (€)	FUEL CELL SYSTEM (€)	BATTERY (€)	TOTAL (€)
1: H2 24 MW	27946.00	470.46	1428.00	854400.00	64947.75	949192.21
2: H2 18 MW	30796.49	471.37	1428.00	640800.00	64947.75	738443.61
3: H2 12 MW	21308.83	356.82	1428.00	427200.00	123710.00	574003.65
4: H2 6 MW	21308.83	229.27	1428.00	213600.00	185565.00	422131.09
5: ONLY BATTERY	-	-	.	.	247420.0	247420.0

Table 0.3.17: Infrastructure manufacturing costs for each configuration.

4.3.5 Section conclusions

Following a comprehensive study of the hydrogen fuel cell power system for a real Hyperloop vehicle, it can be stated that this technology — despite still being in a process of maturation compared to alternatives such as electric batteries — presents a solid proposal, with sufficient technical arguments to merit consideration for demanding real-world applications.

Throughout the analysis, all necessary components have been dimensioned — from hydrogen, oxygen, and water storage tanks to the fuel cell system itself and the support required from the battery. Their weights, volumes, and costs have been examined in detail, comparing various operating configurations.

Upon analyzing the different results, the oversizing of the hydrogen fuel cell system is evident. In all configurations, very high installed power is required to meet acceleration demands, leading to corresponding increases in weight, volume, and cost. However, as installed power is progressively reduced, the battery capacity must be increased to compensate, also resulting in considerable costs and weight.

Hydrogen fuel cell systems are optimal for delivering constant power. When additional power is required for acceleration, this oversizing becomes apparent. Yet if the system were used exclusively for applications without power peaks, it would lead to an oversized battery and inefficient use of the energy available.

From an economic standpoint, a marked difference is observed between the hybrid configurations and the fully battery-electric case. The operational cost of hydrogen-based configurations can exceed that of the pure electric option by more than a factor of twenty, reaching annual figures greater

than 4 million euros in the most demanding cases. Similarly, infrastructure costs exhibit a downward trend as installed hydrogen power is reduced, although even in the most contained case, they remain significantly higher than for the fully electric alternative. The high current operational cost of hydrogen is also a crucial factor that may decisively influence the choice of power system.

Weight and volume analyses confirm the same downward trend. The lower the installed hydrogen power in the fuel cell system, the smaller the H and O storage requirements and the more compact the stack. However, this entails an increase in battery size and mass, as it assumes a more prominent role. Even so, no hybrid configuration matches the structural compactness of the battery-only system.

It is worth emphasizing that the use of hydrogen as a power system remains a technology under development, with extensive research focused on improving efficiency, reducing system weight, and lowering costs. Nevertheless, its implementation involves a significant increase in technological complexity, particularly in terms of safety, as it requires pressurized tanks at 700 bar for H and 200 bar for O, imposing additional demands on design, materials, and risk management. That said, as a green technology — especially when powered by renewable hydrogen — it could gain greater relevance in the future as its advantages are consolidated and cost barriers are overcome.

Finally, given that all configurations require a minimum 525 kWh battery, the modular multistage supercharger designed in the following section could be adjusted in power and configured to supply this battery at the end of each trip in very short charging times.

4.4 Multistage LLC Resonant Supercharger

4.4.1 Introduction

Within the framework of the energy system proposed in Section4.2.5, the need to meet an energy demand of 2 MWh has been identified. This section analyzes the feasibility of implementing a supercharger system as a suitable alternative to recharge a battery capable of supplying the total required energy. This approach allows the complete externalization of the charging infrastructure by locating it at the station, thereby minimizing the on-board weight.

To maximize fleet availability, current long-distance and high-speed trains typically remain at the station for approximately 12 minutes at the end of each trip. During this period, passenger boarding and disembarking must be carried out properly [**?**]. This time constraint, when aiming to charge a Hyperloop train's battery, necessitates the development of a charging technology of exceptionally high power without compromising system efficiency or reliability.

The proposed solution to this challenge is the construction of a charger based on a multistage resonant LLC converter, with a nominal power of 8 MW and a maximum power of 10 MW. With a battery capacity of 2 MWh, this charger would be capable of fully recharging the battery within 10 to 15 minutes, thus meeting the time margins previously indicated. Furthermore, as described in Section 4.2.6, the system employs a lithium-titanate —LTO— battery, a technology that comfortably supports high charging rates —between 4C and 5C—, fully compatible with the intended charger power.

This study includes the analysis, design, and simulation of a multistage resonant LLC charger. To this end, various converter scenarios of this topology were simulated using LTspice, to verify proper operation. Based on the simulation results, a detailed loss and efficiency analysis of the system was carried out, substituting the battery with an equivalent load and examining system performance at various operating points. Additionally, to ensure that the proposal is as realistic as possible, commercial components — such as IGBTs and diodes — were used, with data extracted directly from their respective datasheets.

Finally, an economic study was performed to estimate the implementation cost of the supercharger, to objectively compare it against the other charging technologies analyzed in this work.

4.4.2 Initial Supercharger Design

The resonant LLC converter was selected as the core of this architecture due to its outstanding efficiency in fast-charging applications. This topology enables high switching frequencies and supports soft-switching techniques such as Zero Voltage Switching —ZVS— and Zero Current Switching —ZCS—, which minimize losses and reduce thermal stress on power devices. It is particularly well-suited for managing variable loads — a common feature in battery charging processes — as its control is based on modulation of the resonant tank switching frequency. By increasing or decreasing this frequency relative to the resonant frequency, the converter can effectively regulate the power delivered to the battery, maintaining stable operation even in the presence of voltage fluctuations or load impedance variations. For these reasons, the LLC topology is widely adopted in high-power commercial chargers, known for its compactness, reliability, and operational adaptability.

In addition, the supercharger is designed as a multistage system. This configuration, besides facilitating thermal management of the various components, allows the power to be distributed across multiple parallel branches, avoiding reliance on a single stage. This modularity provides redundancy and enhances system reliability in the event of potential faults. Although this study does not address the detailed design of the protection systems and electrical segmentation, it is important to note that in implementation, elements must be integrated to ensure isolation of the affected stage, allowing the remainder of the system to continue operating safely.

Regarding the specified operating conditions, under nominal load at 8 MW, the charger will deliver power to the battery at 5000 V and 1600 A. This current will be divided among the various power stages detailed later. Given the gain regulation capability offered by this charger topology, different operating points have been analyzed, varying the gain for both nominal and maximum power, to identify the most demanding conditions.

It should be reiterated, as discussed in Section 4.2.6 , that the detailed design of the battery topology is beyond the scope of this study — that is, it does not address the specific series-parallel cell configuration or the battery management system —BMS—.

It is also crucial to emphasize that the LTspice simulation performed focuses exclusively on the behavior of the resonant LLC converter, starting from the stage immediately prior to switching, where a DC input voltage of 2500 V is applied.

To provide context and support the technical explanations that will follow, the figure below presents an image extracted from LTspice showing the complete topology of the converter.

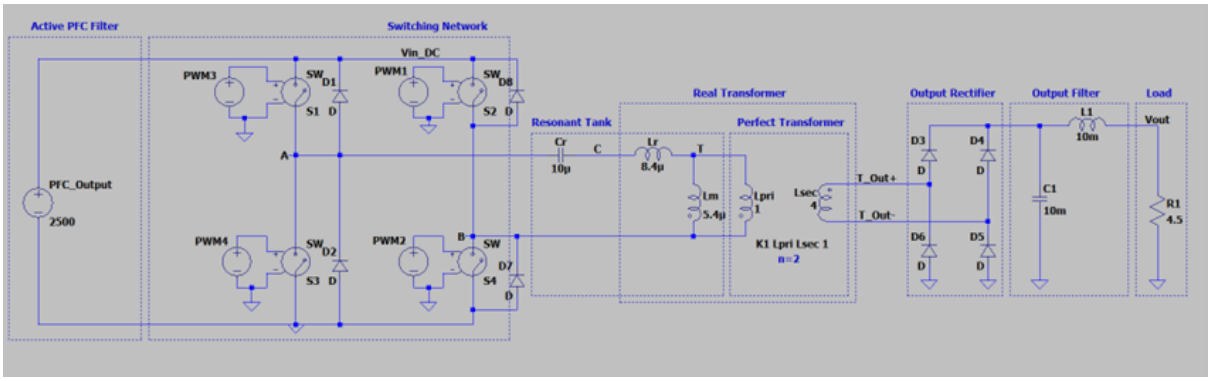

Figure 0.4.1: Diagram of the converter implemented in LTspice.

The image illustrates the different functional blocks that comprise a resonant LLC converter. These are: the switching stage, the resonant tank, the transformer, the output rectifier, and an LC filter positioned before the battery.

In summary, starting from 2500 V DC, the switching stage generates a square wave signal that drives the resonant LLC tank. In response, the tank produces a resonant sinusoidal current, which is subsequently stepped up by a transformer with a 1:2 turns ratio and rectified in the output stage. Finally, an output capacitor filters out the AC component, delivering a stabilized DC voltage to the battery.

The figure represents a single 8 MW stage. One of the key advantages of LTspice is that it enables simulation of the system's full power through a single stage, which facilitates observation of the total currents passing through each component. These values can later be scaled according to the total number of stages and the number of IGBTs arranged in parallel. From this point onward, each section of the resonant converter is explained in detail.

Before addressing in detail the operation of the resonant converter, the stages preceding its input are briefly described, with particular emphasis on the process by which the required 2500 V DC is achieved. It should be noted that these stages were not simulated, as their inclusion exceeds the scope of this work; however, their explanation is necessary for a comprehensive understanding of the system.

4.4.2.1 Preliminary Stages Prior to the LLC Converter

The charging system designed for the Hyperloop vehicle is powered by standard railway electrical substations, supplying 25 kV AC three-phase at 50 Hz — a specification common across high-speed rail networks in Europe and Japan. The substations considered in this study were:

- Madrid Puerta de Atocha Station, Spain
- Gare de Lyon, Paris, France
- Bruxelles-Midi / Brussel-Zuid Station, Brussels, Belgium
- Shinagawa Station, Tokyo, Japan — supplying the Maglev Shinkansen, which employs technology similar to that of Hyperloop

The AC voltage is stepped down by a medium-voltage transformer and rectified via a three-phase full-wave bridge to produce 2500 V DC, the input for the resonant LLC converter. An active power factor correction —PFC— stage ensures near-unity power factor and reduced harmonic distortion, while a DC filter stabilizes the output. EMI filters protect both the grid and the system electronics from switching noise.

Due to the length constraints of this work, these stages are not developed in further detail. However, a general overview is provided to offer context and clarity on the complete system architecture. For the purposes of this study, these stages are assumed to operate ideally, delivering stabilized 2500 V DC to the LLC converter without significant losses.

4.4.3 Analysis of the LLC Converter Stages

The following section provides a detailed analysis of the design and operation of each stage that constitutes the resonant LLC converter.

First, the operation and associated calculations of the resonant tank are explained. Although this stage is located after the switching stage, it is essential to address it first, as its behavior directly influences the results obtained in both the switching and rectification stages. Therefore, before presenting and analyzing the corresponding simulations of those stages, the resonant tank is developed in detail.

4.4.3.1 LLC Resonant Tank

Subsequently, we find the key element of the LLC converter — the so-called resonant tank. This tank consists of a series inductance —Lr—, a magnetizing inductance —Lm—, and a capacitor —Cr—. Together, these components define the dynamic behavior of the system and the method by which power is regulated. Its main function is to transform the square wave generated by the inverter into a sinusoidal signal, which is much better suited for subsequent rectification. By adjusting the switching frequency relative to the resonant frequency, the tank allows control of the output power without altering the duty cycle — a particularly useful feature when charging a battery, where impedance changes during the process. In practice, this means operating with a switching frequency close to the resonant frequency to deliver more power, or farther from it to reduce power, always operating above resonance. A primary design objective in LLC resonant converters is to achieve efficient switching, minimizing losses linked to voltage and current transients. This is accomplished through soft-switching techniques — most notably Zero Voltage Switching —ZVS— and Zero Current Switching —ZCS—. ZVS enables power switches — in this study, IGBTs — to turn on when the voltage across their terminals is negligible. Technically, this means the turn-on loss energy —Eon— approaches zero. This condition is achieved by using the energy stored in the inductive and parasitic elements of the circuit to fully discharge the switch capacitance before activation. Reducing Eon is particularly important for IGBTs, as their switching losses are concentrated during turn-on. Achieving ZVS not only minimizes dynamic losses but also reduces heat generation, simplifying cooling and improving overall efficiency. ZCS is typically applied to output diodes or synchronous rectifiers, ensuring that the device turns off when the current through it is near zero. This reduces reverse recovery losses — critical in fast diodes — and protects components from unnecessary electrical stress. Overall, implementing soft switching through ZVS and ZCS in

the various stages of the LLC resonant converter optimizes performance, extends service life, and ensures efficient operation in high-frequency, high-power applications.

4.4.3.2 Resonant Tank Gain Analysis

In order to design the resonant tank, it is crucial to calculate four key elements — the resonant frequency —fr—, the resonant or parasitic inductance —Lr—, the magnetizing inductance —Lm—, and the resonant capacitance —Cr—.

As previously discussed, the objective is to analyze the charger at different operating points. The main advantage of the LLC converter is its ability to adjust voltage gain by modulating the switching frequency. In practice, these converters are designed to operate with voltage gains between 0.8 and 1.2 relative to the nominal output voltage.

For this study, starting from a nominal voltage of 5000 V, the converter has been dimensioned to operate stably within an output voltage range from 4000 V to 6000 V.

An illustrative diagram of the resonant tank is presented below:

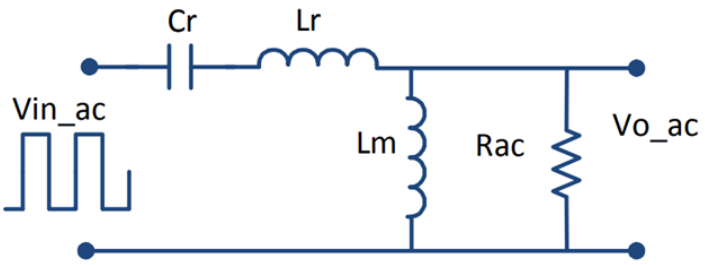

Figure 0.4.2: Illustrative diagram of the resonant tank operation.

To define these values, the resonant tank gain must first be plotted. After generating representative gain curves while varying the load across the tank, an iterative process was carried out, adjusting the values and ratio between the two inductances and the capacitance, until achieving curves that accurately reflect the desired behavior of the resonant tank.

The total gain $G(\omega)$ of an LLC converter can be expressed as:

$$G = p \cdot n \cdot K \tag{4.1}$$

Where:

- **p** is the gain of the switching bridge — 1 for full bridge, 0.5 for half bridge
- **n** = N_p/N_s is the transformer turns ratio
- **K(ω)** is the resonant tank gain, which depends on angular frequency ω, the load, and the tank components, and is defined as:

$$K(\omega) = \frac{Z_{lp}(\omega)}{Z_r + Z_{lp}(\omega)} \tag{4.2}$$

The tank gain consists of two elements. The first is the series impedance of the resonant inductance and capacitance:

$$Z_r(\omega) = j\omega L_r + \frac{1}{j\omega C_r} \tag{4.3}$$

The second is the load impedance — representing the battery — in parallel with the magnetizing inductance:

$$Z_{lp}(\omega) = \frac{R_{ac} j\omega L_m}{R_{ac} + j\omega L_m} \tag{4.4}$$

These values will be further detailed later, when explaining how to obtain the resonant tank gain curves.

To proceed with understanding these concepts, it is necessary to consider the following definitions and their influence:

- **Q** — quality factor Losses are related to the quality factor Q — where higher Q corresponds to lower energy loss ratio.

$$Q = \frac{\sqrt{L_r/C_r}}{R_{ac}} \tag{4.5}$$

- **Rac** — reflected load impedance This refers to the secondary load of the transformer — in this case, the battery — as seen from the primary side:

$$R_{ac} = \frac{8}{\pi^2} \cdot \frac{N_p^2}{N_s^2} \cdot R_o = \frac{8}{\pi^2} \cdot \frac{N_p^2}{N_s^2} \cdot \frac{V_{out}^2}{P_{out}} \tag{4.6}$$

- **fr** — resonant frequency Represents the optimal operating frequency at unity gain:

$$f_r = \frac{1}{2\pi\sqrt{L_r \cdot C_r}} \tag{4.7}$$

- **m** — inductance ratio Represents the ratio of the total primary inductance to the resonant inductance:

$$m = \frac{L_r + L_m}{L_r} \tag{4.8}$$

- **Fx** — normalized switching frequency Represents the ratio between the switching frequency and the resonant frequency:

$$F_x = \frac{f_{sw}}{f_r} \tag{4.9}$$

Prior to the design, it was decided to locate the resonant frequency between 15 kHz and 20 kHz, which are typical switching frequencies for IGBTs in high-power applications.

The following figure illustrates a key behavior for understanding LLC converter operation. When plotting gain curves for various load levels, two distinct regions can be observed — the capacitive region and the inductive region.

The peak of each curve — corresponding to a specific load condition — defines the boundary between these regions, known as the minimum switching frequency. Frequencies below the peak of the curve associated with the lightest load define the capacitive region, while frequencies above the peak correspond to the inductive region.

The requirement to operate under ZVS — as previously discussed — is met only in the inductive region. If the converter operates within the capacitive region, the soft-switching condition is lost, leading to an increase in reverse recovery losses — particularly critical in IGBTs — and a significant reduction in overall system efficiency.

The following figure illustrates the three possible operating modes [4]:

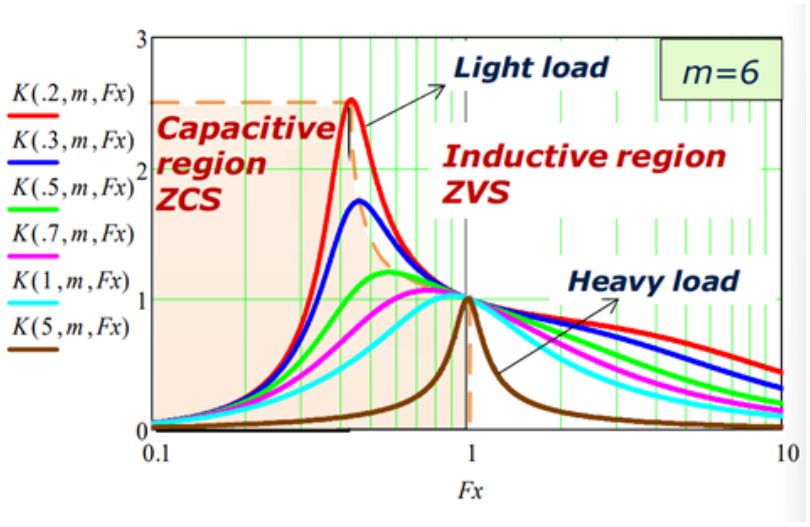

Figure 0.4.3: Illustration of the capacitive and inductive regions and possible operating modes of the LLC converter.

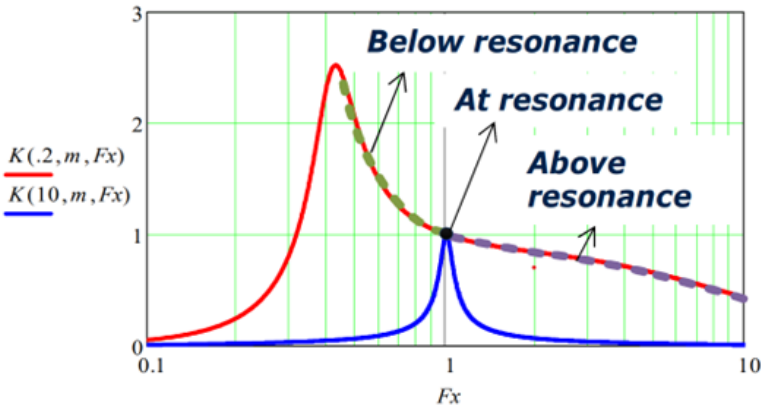

Figure 0.4.4: Illustration of the three possible operating modes of the LLC converter.

These modes are:

- Operating at the switching frequency corresponding to unity gain — $f_{sw} = f_r$
- Operating above the resonant frequency, achieving higher gain — $f_{sw} > f_r$
- Operating below the resonant frequency, achieving lower gain — $f_{sw} < f_r$

It is important to emphasize that, when deriving the gain curves, the objective is to ensure that within the established gain limits — 0.8 to 1.2 — there exists a sufficiently wide frequency range that enables proper modulation of the converter for each desired operating point.

The gain curves obtained for this study, corresponding to three different load levels, are presented below:

Figure 0.4.5: Resonant tank gain curves at different load levels.

The blue curve represents the gain of the resonant tank under nominal conditions — delivering 8 MW at 5000 V and 1600 A.

The grey curve corresponds to a light load — 200 A — where the system demand is minimal.

The orange curve reflects the most demanding condition — 2500 A load corresponding to 10 MW at 4000 V.

As previously mentioned, the design criterion is for the resonant tank gain to remain within the range of 0.8 to 1.2, and for this entire range to fall within the inductive region.

It can be observed from the graph that the minimum switching frequency — the peak of the curve — even under the most demanding condition — orange curve — lies above a gain value of 1.2. Specifically, the peak occurs at a gain of approximately 1.25.

This ensures that, even for the highest load, the entire desired gain range remains within the inductive region. Therefore, the condition for soft switching — ZVS — is met without compromising any operating point. From this limiting case, it can be inferred that all less demanding load conditions will also satisfy the minimum switching frequency margin.

4.4.3.3 Methodology for Gain Curve Plotting

The following explains how the final gain curves shown in the previous section were generated.

The iterative method consists of adjusting the values of L_r, L_m, and C_r until the resulting curves meet the design requirements described earlier. Once the correct values are identified, other parameters — such as the resonant frequency — are derived from the equations previously presented.

To plot the curves, the frequency space is divided into very small increments x, allowing the gain to be calculated at each point across the range. The division follows:

$$x = 10^{1/100} \tag{4.10}$$

The switching frequency at each point is then calculated:

$$f_{sw} = f_r \cdot x \tag{4.11}$$

From this, the switching angular frequency is determined:

$$\omega_{sw} = 2\pi \cdot f_{sw} \tag{4.12}$$

Using this value, the reactances of the magnetizing inductance, resonant inductance, and resonant capacitance are computed:

$$X_{Lm} = \omega_{sw} \cdot L_m \tag{4.13}$$

$$X_{Lr} = \omega_{sw} \cdot L_r \tag{4.14}$$

$$X_{Cr} = \frac{1}{\omega_{sw} \cdot C_r} \tag{4.15}$$

These allow calculation of the gain magnitude at each point, as described earlier:

$$K(\omega) = \frac{Z_{lp}(\omega)}{Z_r(\omega) + Z_{lp}(\omega)} \tag{4.16}$$

Finally, the table below presents the resonant tank design values for a single stage rated between 8 and 10 MW. This design is intended for LTspice implementation, from which the complete system behavior can be simulated. The resulting current values can then be distributed according to the number of stages connected in parallel, as defined in the final charger architecture.

Table 0.4.1: Resonant tank design values for 8–10 MW power stage

Parameter	Value	Units
L_m	5.40 E-6	H
L_r	8.40 E-6	H
C_r	10.00 E-6	F
m	1.643 E+0	Scalar
f_r	17.37 E+3	Hz
L_r/C_r	840.00 E-3	Scalar
$\ln(L_m/L_r)$	642.86 E-3	Scalar
$F_{\min}$	15480	Hz
R_{ac} 8 MW	0.633	Ω
R_{ac} 10 MW	0.507	Ω
Q 200 A	0.181	Scalar
Q 1600 A	1.447	Scalar
Q 2500 A	2.261	Scalar

By introducing the tank values into LTspice, the currents passing through a single 8 MW stage under nominal conditions can be observed:

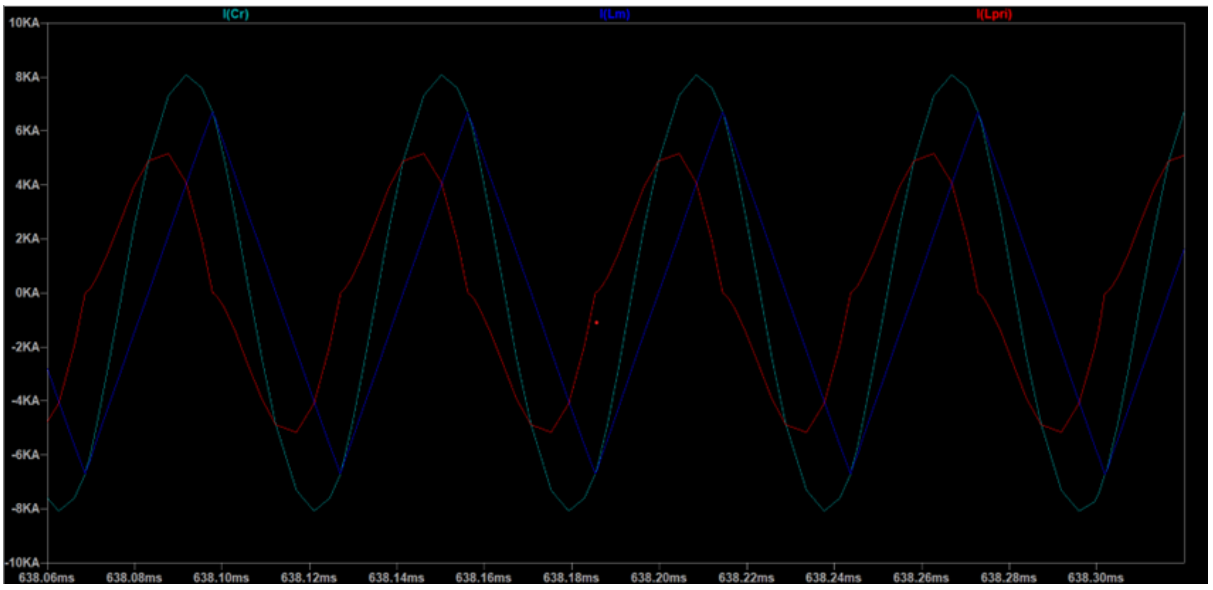

Figure 0.4.6: LTspice simulation of the currents in the resonant tank under nominal conditions.

As shown in the simulation, the current through the transformer is divided into two components — one flows through the magnetizing inductance L_m, and the other through the primary winding inductance L_{pri}. This distribution is characteristic of the resonant behavior in LLC topologies. As previously explained, the current values obtained will later be scaled according to the total number of parallel-connected stages.

Regarding the voltages seen by the tank, these are illustrated in the following figure:

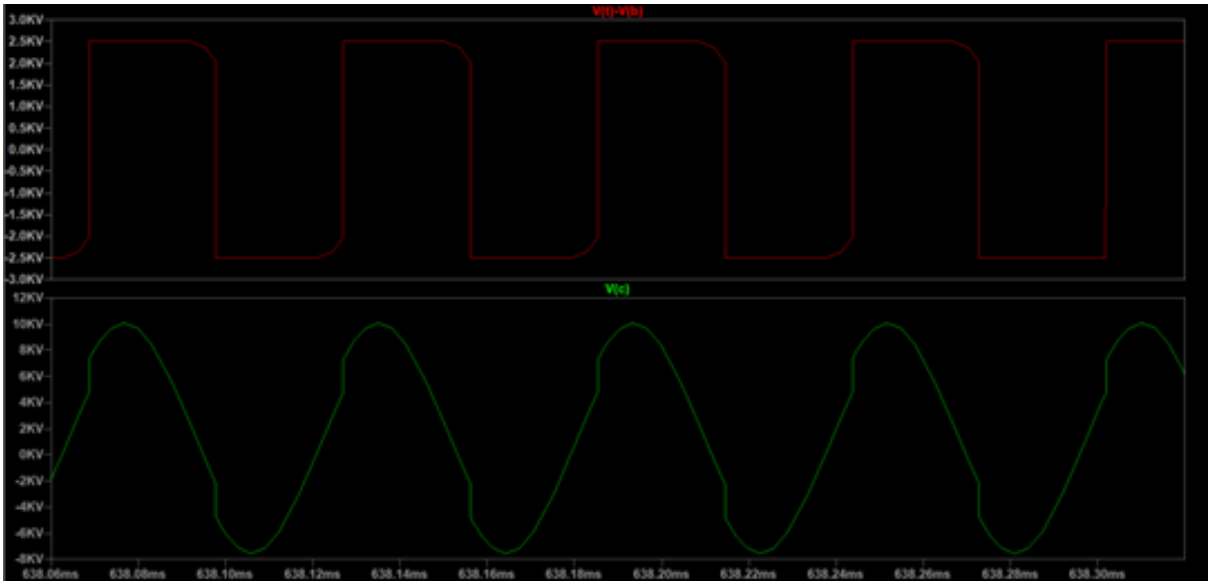

Figure 0.4.7: LTspice simulation of the voltages in the resonant tank.

The graph reveals two key signals. The red trace represents the output of the full-bridge IGBT stage. Starting from a 2500 V DC input, this generates an alternating square wave between -2500 V and $+2500$ V, applied directly to the tank.

The resonant tank operates correctly, producing a sinusoidal voltage at the applied switching frequency, closely matching the resonant frequency.

4.4.3.4 Switching Stage Design And Results

The first stage, starting from a constant DC voltage, corresponds to the switching stage, implemented using a full-bridge of IGBTs. This bridge converts the DC input voltage into a square wave that subsequently drives the resonant tank.

Regarding the choice of transistor, IGBTs were selected over MOSFETs due to their higher voltage blocking capability, superior performance at high power, and efficient conduction at low switching frequencies — all essential characteristics for this type of converter.

The device selected for this function is the Infineon FZ1200R33HE3, featuring a maximum collector-emitter voltage — V_{CE} — of 3300 V and a nominal current rating of 1200 A.

To analyze the converter's behavior under realistic conditions, six operating points were evaluated — three voltage levels —0.8, 1.0, and 1.2 times the nominal 5000 V— combined with two power levels —8 MW and 10 MW—. From these voltage and power values, the equivalent load resistance represented by the battery, as well as the corresponding current for each case, were calculated. This resistance follows:

$$R = \frac{V_{out}^2}{P_{out}} \tag{4.17}$$

These results, along with the resonant and switching frequencies, are summarized in the following table:

Table 0.4.2: Battery modelation as a resistance at different operating points

DESIRED POWER 8 MW			
Parameter	**0.8 * V_{NOM}**	V_{NOM}	**1.2 * V_{NOM}**
Voltage (V)	4000	5000	6000
Resistance (Ω)	2	3.125	4.5
Current (A)	2000	1600	1333.33
FSW (Hz)	18140	17140	16210
F. Resonance (Hz)	18700	17370	16440
DESIRED POWER 10 MW			
Voltage (V)	4000	5000	6000
Resistance (Ω)	1.6	2.5	3.6
Current (A)	2500	2000	1666.67
FSW (Hz)	19040	17140	16210
F. Resonance (Hz)	18700	17370	16440

As observed, the switching frequency and resonant frequency exhibit slight variations between operating points. These differences are due to the inherent losses of the IGBTs, which require the switching frequency to be slightly reduced in order to achieve higher voltage gain and properly deliver the required power under high load conditions.

Regarding the LTspice simulation, the square voltage waveform corresponds to that shown in the previous section. The currents for a single 8 MW stage at 5000 V are shown below:

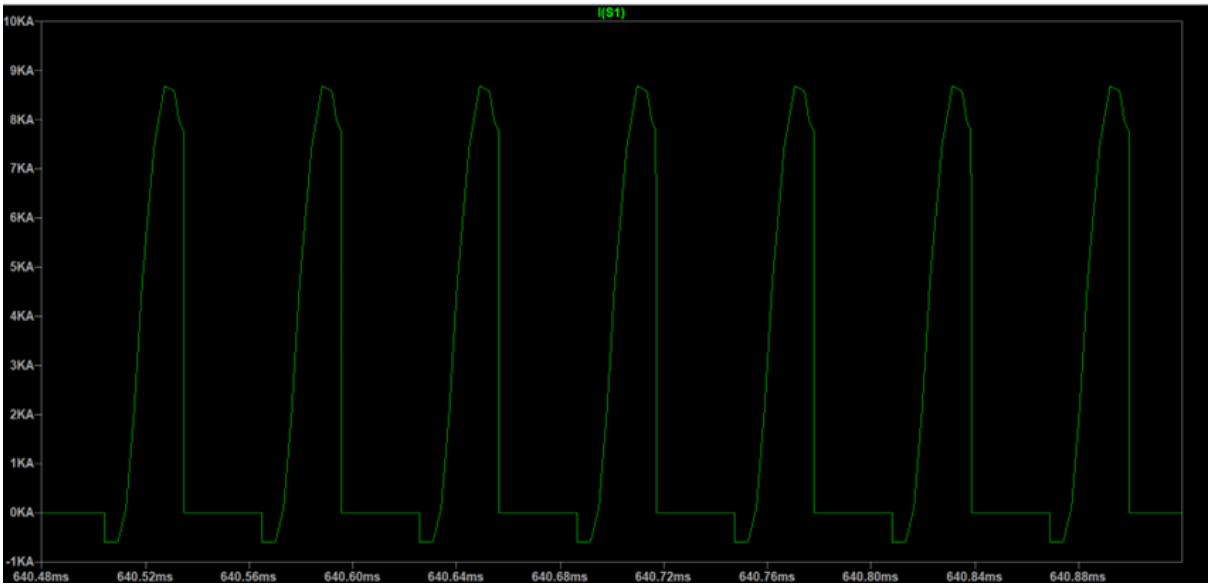

Figure 0.4.8: LTspice simulation of the switching current for a single 8 MW stage at 5000 V.

It is worth noting that the current shown in the figure never takes negative values, as it represents only the current through the ideal switch. In a real IGBT, conduction during the negative part of the cycle would be handled by the antiparallel diode, which is not represented in this curve.

The following table summarizes the values obtained from the LTspice simulations for the different charger operating points, along with the most relevant parameters from the selected IGBT's datasheet. The table is color-coded: in the LTspice section, white cells represent direct simulation results for a single stage at different operating points, while green cells correspond to the current through each individual IGBT, considering the total number of parallel-connected stages — in this case, 8 stages — representing a scenario where each stage operates in the range of 1 to 1.25 MW. In these cases, the current through each IGBT, for n stages and m IGBTs in parallel, is:

$$I_{IGBT} = \frac{I_{total}}{n \cdot m} \tag{4.18}$$

The peak, average, and RMS currents flowing through the IGBTs, as calculated from the simulations, are presented below.

In the lower section, the most representative data from the datasheet of the Infineon FZ1200R33HE3 model are included. The white values are taken directly from the manufacturer's documentation, while the green-highlighted values have been derived from other data within the same document.

One key parameter is the dynamic resistance R_{on}, which represents the internal conduction resistance of each IGBT. This value was manually entered into the LTspice simulation model and is calculated as:

$$R_{on} = \frac{V_{CE}}{I_C} \tag{4.19}$$

The V_{CE} values were obtained from the following datasheet graph at $T_{vj} = 125\,$ºC:

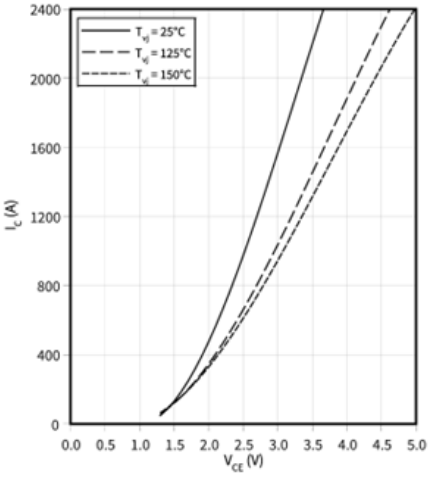

Figure 0.4.9: Extract from the Infineon FZ1200R33HE3 datasheet showing V_{CE} at $T_{vj} = 125\,$ºC.

The summary table is presented below:

LLC RESONANT CONVERTER	NOM 8MW 5000V 1600A	8MW 4000V 2000A	8MW 6000V 1333.3A	10 MW 5000V 2000A	10 MW 4000V 2500A	10MW 6000V 1666.6 A
Fsw (Hz)	17140	18140	16210	17140	17494	16210
Vout (V)	5000	4000	6000	5000	4000	6000
Nº STAGES	8					
LTSPICE IGBT VALUES						
Nº IGBTs in PARALLEL	1	1	1	1	1	1
TOTAL Nº IGBTs	32	32	32	32	32	32
I RMS SWITCHING TOTAL (A)	3743.40	3572.80	3918.60	4094.00	4210.20	4308.80
I RMS / IGBT (A)	467.93	446.60	489.83	511.75	526.28	538.60
I PEAK (A)	7800.00	7800.00	8400.00	8600.00	8800.00	9060.00
I PEAK/IGBT (A)	975.00	975.00	1050.00	1075.00	1100.00	1132.50
I AVG (A)	1929.56	1889.66	2057.20	2262.40	2298.20	2357.60
I AVG/IGBT (A)	241.20	236.21	257.15	282.80	287.28	294.70
DATASHEET IGBT VALUES INFINEON 3300V 1200A						
Ic NOM (A)	1200	1200	1200	1200	1200	1200
VCE NOM (V)	2100	2100	2100	2100	2100	2100
VDC Link (V)	2500	2500	2500	2500	2500	2500
VCE for IRMS (V)	3.8	4.1	4.1	4.1	4.2	4.2
VCE for IRMS / IGBT (V)	1.8	1.8	1.8	1.8	1.8	1.8
Ron (miliOhmn)	1.015	1.148	1.046	1.001	0.998	0.975
Ron / IGBT (miliOhmn)	3.847	4.030	3.675	3.517	3.420	3.342
Ron (Ohmn)	0.00102	0.00115	0.00105	0.00100	0.00100	0.00097
Ron / IGBT (Ohmn)	0.00385	0.00403	0.00367	0.00352	0.00342	0.00334
VCEO (V)	0.9	0.9	0.9	0.9	0.9	0.9
Eon (mJ) -ZVS-	0	0	0	0	0	0
Eoff (mJ)	1800	1800	1800	1800	1800	1800
Eon (J)	0	0	0	0	0	0
Eoff (J)	1.8	1.8	1.8	1.8	1.8	1.8

Figure 0.4.10: Summary of LTspice simulation currents and key parameters of the selected IGBT at different operating points.

The E_{on} value is zero due to the achievement of ZVS, as explained previously.

Furthermore, it is evident that the selected IGBT — with a nominal current rating of $I_C = 1200$ A — is capable of handling the 975 A peak current passing through the device under nominal conditions, when considering 8 parallel stages, without exceeding its limit.

These current peaks are not directly associated with the load, but rather result from the intrinsic behavior of the LLC resonant tank. In this topology, the circulating current is neither purely DC nor proportional to the output; instead, it is generated by the excitation of the resonant circuit formed by L_r, C_r, and L_m. This oscillatory current — known as the resonant current — exhibits a high-amplitude sinusoidal waveform, even in the absence of a heavy load.

4.4.3.5 Rectification Stage and LC Filter: Design And Results

First, following the resonant tank is a transformer with a 1:2 turns ratio, which doubles the voltage from 2500 V to 5000 V prior to the rectification stage.

The rectification stage — responsible for converting the AC signal to DC — consists of a full-bridge of diodes. The diodes selected for this purpose are manufactured by Dynex, model DRD4690H85.

It is important to note that very few commercially available diodes can simultaneously withstand the high voltages and currents required by this system. The selected model supports a repetitive peak reverse voltage — V_{RRM} — of 8500 V and a continuous current of 4690 A, making it a suitable choice for this high-power application.

The following table presents the results obtained directly from LTspice simulations, along with the most relevant parameters extracted from the diode's datasheet:

LLC RESONANT CONVERTER	NOM 8MW 5000V 1600A	8MW 4000V 2000A	8MW 6000V 1333.3A	10 MW 5000V 2000A	10 MW 4000V 2500A	10MW 6000V 1666.6 A
LTSPICE DIODE VALUES						
Nº TOTAL DIODES	4	4	4	4	4	4
I RMS DIODE (A)	1227.06	1494.04	1073.80	1595.50	1865.06	1316.00
I AVG DIODE (A)	777.68	960.58	637.46	993.76	1200.32	803.30
REAL I RMS DIODE (A)	153.38	186.76	134.23	199.44	233.13	164.50
REAL I AVG DIODE (A)	97.21	120.07	79.68	124.22	150.04	100.41
DATASHEET VALUES DIODE DYNEX 8500V 4690 A						
Qs (uC)	12000	12000	12000	12000	12000	12000
Qs (C)	0.012	0.012	0.012	0.012	0.012	0.012
Erec (J)	1.2	1.2	1.2	1.2	1.2	1.2
rt (miliOhmn)	0.11	0.42	0.42	0.42	0.42	0.42
rt (Ohmn)	0.00011	0.00042	0.00042	0.00042	0.00042	0.00042
VDO (V)	1.15	1	1	1	1	1
VT (V)	100	100	100	100	100	100

Figure 0.4.11: Summary of LTspice simulation currents and key parameters of the selected diode at different operating points.

Following the same approach used in the switching stage analysis, the white values represent simulation results for a single 8 MW stage. The green values indicate the current through each individual diode if the system were divided into 8 parallel-connected stages. This division is based on the following formula for n stages:

$$I_{diode} = \frac{I_{total}}{n} \tag{4.20}$$

Additionally, the datasheet values will be crucial for calculating losses and the total system efficiency in the next section.

As an example, the following figure shows current waveforms in two of the diodes in the bridge, corresponding to a single 8 MW stage simulation at 5000 V. As can be seen, the diodes conduct alternately in complementary fashion, as expected in an LLC bridge rectifier:

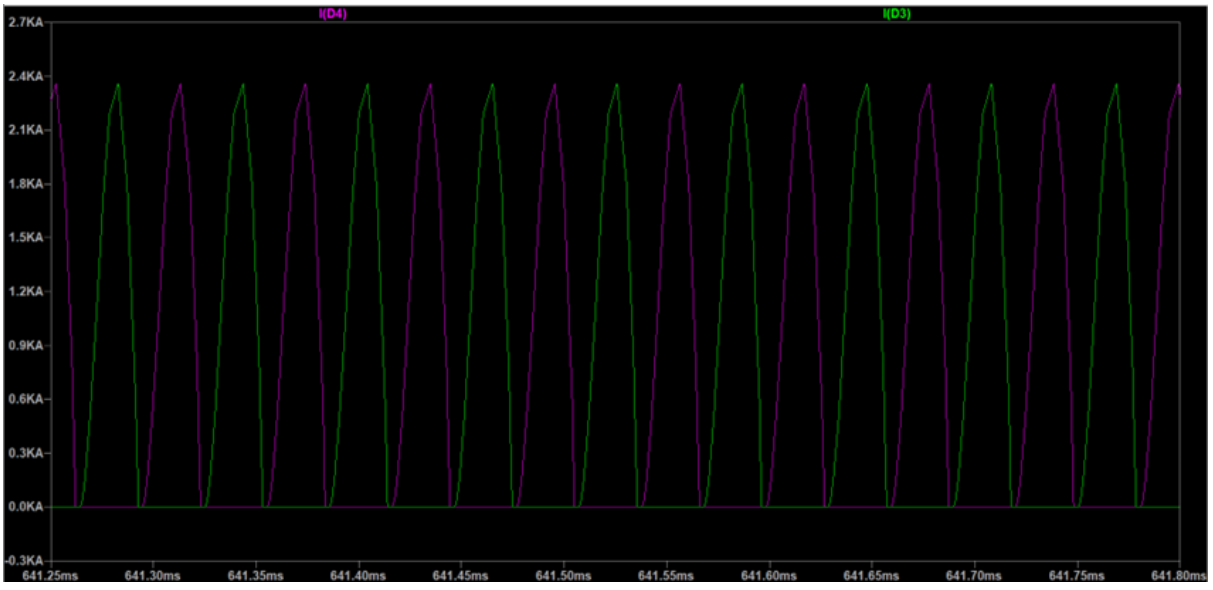

Figure 0.4.12: LTspice simulation of diode currents in the rectifier bridge at 5000 V for a single 8 MW stage.

Finally, immediately before connection to the battery, an LC filter is incorporated. Its purpose is to smooth out the ripple present in the output voltage and current of the converter. This low-pass filter, with a cutoff frequency of 16 Hz, ensures that the battery receives a stable DC signal, free from high-frequency oscillations that could negatively impact both its service life and charging efficiency.

The filter values were determined experimentally, achieving optimal performance across all simulations. In all cases, virtually no ripple was observed in the output voltage, validating the choice of components. The selected values were 10 mH for the inductance and 10 mF for the capacitance.

The following graph presents a detailed view of the steady-state response at the converter output. The green trace shows the constant DC voltage applied to the battery, while the red trace represents the charging current, also constant. The results correspond to a simulation of an 8 MW converter under nominal conditions:

Figure 0.4.13: LTspice simulation of output voltage and current applied to the battery under nominal conditions for an 8 MW stage.

4.4.4 Losses, Efficiency and Thermal Study

From this point onward, the calculation of losses as a function of the selected number of stages is developed, applying the analysis to the six operating points defined previously. Based on these calculations, the corresponding efficiency for each case will be determined.

Additionally, this section includes the thermal study of the system, with the aim of jointly comparing the results obtained. This approach reflects the fact that, while certain configurations may exhibit superior electrical efficiency, they lose all viability if they are not thermally sustainable. Therefore, both analyses must be considered together to provide a complete and realistic evaluation of the system.

4.4.4.1 Explanation of Loss and Efficiency Calculations

When evaluating losses in an LLC resonant converter, they are divided into two main categories: conduction losses and switching losses, both for the IGBTs and the diodes.

The values used in the following formulas are compiled in the summary tables presented in the previous section for both the switching stage and the rectification stage.

In summary, conduction losses occur when the device is in the 'on' state and conducting current, and are proportional to the R_{on} value and the square of the current. Switching losses, on the other hand, occur during the device's turn-on and turn-off transitions, and depend on the parameters E_{on} and E_{off}, as well as the switching frequency [17].

Starting with the IGBT conduction losses, these are given by the following formula:

$$P_{\text{cond}}^{\text{IGBT}} = V_{\text{CE0}} \cdot I_{\text{AVG}} + R_{\text{on}} \cdot I_{\text{RMS}}^2 \tag{4.21}$$

And, for the diode:

$$P_{\text{cond}}^{\text{Diode}} = V_{\text{D0}} \cdot I_{\text{AVG}} + R_{\text{D0}} \cdot I_{\text{RMS}}^2 \tag{4.22}$$

Where:

- $P_{\textbf{cond}}^{\textbf{IGBT}}$ — conduction losses in the IGBT —W—
- $V_{\textbf{CE0}}$ — collector-emitter threshold voltage during conduction —V— obtained from the graph shown previously at $I_C = 0$ A
- $R_{\textbf{on}}$ — dynamic on-state resistance of the IGBT —Ω—
- $I_{\textbf{AVG}}$ — average current through the IGBT —A—
- $I_{\textbf{RMS}}$ — RMS current through the IGBT —A—
- $P_{\textbf{cond}}^{\textbf{Diode}}$ — conduction losses in the diode —W—
- $V_{\textbf{D0}}$ — forward voltage drop of the diode —V— obtained from the datasheet graph at $I_F = 0$ A
- $R_{\textbf{D0}}$ — dynamic on-state resistance of the diode —Ω— equivalent to r_t in the previous summary table

Next, switching losses are addressed. For the IGBTs, the losses are calculated as

$$P_{\text{sw}}^{\text{IGBT}} = (E_{\text{on}} + E_{\text{off}}) \cdot f_{\text{sw}} \cdot \frac{I_{\text{AVG}}}{I_{\text{NOM,IGBT}}} \cdot \frac{V_{\text{DC Link}}}{V_{\text{NOM,IGBT}}} \tag{4.23}$$

And for the diodes:

$$P_{\text{sw}}^{\text{Diode}} = E_{\text{rec}} \cdot f_{\text{sw}} \cdot \frac{I_{\text{AVG}}}{I_{\text{NOM,Diode}}} \cdot \frac{V_{\text{DC Link}}}{V_{\text{NOM,Diode}}} \tag{4.24}$$

Where:

- $P_{\textbf{sw}}^{\textbf{IGBT}}$ — switching losses in the IGBT —W—

- $P_{\mathbf{sw}}^{\mathbf{Diode}}$ — reverse recovery losses in the diode —W—
- $E_{\mathbf{on}}$ — energy dissipated by the IGBT at each turn-on —J—
- $E_{\mathbf{off}}$ — energy dissipated by the IGBT at each turn-off —J—
- $E_{\mathbf{rec}}$ — reverse recovery energy dissipated by the diode —J—
- $f_{\mathbf{sw}}$ — switching frequency —Hz—
- $I_{\mathrm{NOM,IGBT}}$ — current used by the manufacturer to measure switching losses of the IGBT, as specified in the datasheet —1200 A—
- $I_{\mathrm{NOM,Diode}}$ — current used by the manufacturer to measure switching losses of the diode, as specified in the datasheet —4690 A—
- $V_{\mathbf{DC\ Link}}$ — DC link bus voltage —V—
- $V_{\mathrm{NOM,IGBT}}$ — voltage used by the manufacturer to measure switching losses, as specified in the datasheet —3300 V—
- $V_{\mathrm{NOM,Diode}}$ — voltage used by the manufacturer to measure switching losses, as specified in the datasheet —8500 V—

It should be noted that the loss values presented so far correspond to a single diode or IGBT. Therefore, to determine the total losses — both conduction and switching — these values must be multiplied by the number of devices per stage and by the total number of stages connected in parallel.

In addition, for a comprehensive analysis of total system losses, other elements not yet considered must also be accounted for: losses associated with the transformer, the resonant tank's capacitors and inductors, and the output capacitor.

According to various technical studies of high-power LLC resonant converters, these additional losses are estimated to represent approximately 21.4% of the total. The percentage breakdown of these contributions is shown in the following table [18]:

Table 0.4.3: Power loss ratio per component

Power loss ratio per component (%)	Value
Winding primary transformer	6
Winding secondary transformer	5
Resonant capacitor	1.7
Resonant inductor	1.7
Output capacitor	7
TOTAL	21.4

The efficiency of the converter is defined by the following expression:

$$\text{Efficiency}\ (\%) = \frac{P_{\text{out}}}{P_{\text{out}} + P_{\text{loss}}} \cdot 100 \tag{4.25}$$

4.4.4.2 Thermal Study Methodology

This section develops the necessary calculations to verify whether the various components of the converter — IGBTs and diodes — are thermally viable under the selected stage configuration. The total losses dissipated by each component are analyzed, and the junction temperature reached under continuous operating conditions is evaluated. This analysis confirms whether the devices operate within the thermal limits specified by the manufacturer, thus ensuring reliability and safety during prolonged operation.

The heat transfer of these components is modeled as an equivalent electrical circuit. The following figure illustrates this circuit:

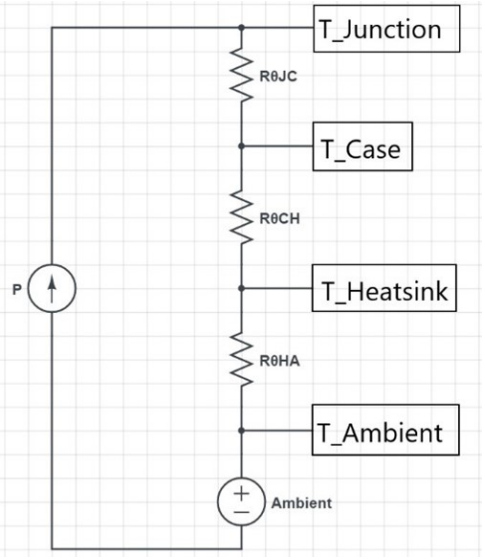

Figure 0.4.14: Equivalent thermal circuit model for heat transfer analysis.

This circuit includes the following thermal resistances:

- $R_{\text{th\_jc}}$ — Junction-to-case thermal resistance Represents the resistance to heat flow from the device's internal junction —T_j— to the case surface —T_c—.
- $R_{\text{th\_ch}}$ — Case-to-heatsink thermal resistance Represents the thermal resistance between the base of the case and the heatsink, including the thermal interface material —TIM— — such as thermal grease.
- $R_{\text{th\_ha}}$ — Heatsink-to-ambient thermal resistance Represents the ability of the heatsink to transfer heat to the surrounding air.

For the calculations, the maximum junction temperature specified by the manufacturer has been adopted for both the IGBT and the diode — 150 ºC. The ambient temperature is conservatively set at 50 ºC to ensure a thermally robust design.

The $R_{\text{th\_jc}}$ and $R_{\text{th\_ch}}$ values are provided by the manufacturer in the respective datasheets. To determine whether the system is thermally viable, the value of $R_{\text{th\_ha}}$ must be calculated. A negative $R_{\text{th\_ha}}$ indicates that the component would exceed its maximum allowable temperature, making the design thermally unfeasible. Conversely, if $R_{\text{th\_ha}}$ is positive, the component operates within the safe thermal margins specified by the manufacturer.

The manufacturer's specified values for both the IGBT and the diode are as follows:

Table 0.4.4: Thermal study values from Infineon IGBT 3300V 1200A datasheet

Parameter	Value
$R_{\text{thJ-C}}$ (K/kW)	9.55
$R_{\text{thC-H}}$ (K/kW)	10
T_j (K)	398
T_{amb} (K)	323

Table 0.4.5: Thermal study values from diode 8500V datasheet

Parameter	Value
$R_{\text{thJ-C}}$ (ºC/W)	0.022
$R_{\text{thC-H}}$ (ºC/W)	0.004
T_j (ºC)	160
T_{amb} (ºC)	50

The expression for calculating $R_{\text{th\_ha}}$ for both the IGBT and the diode is:

$$R_{\text{th\_ha}} = \frac{T_j - T_a}{P_{\text{loss}}} - R_{\text{th\_jc}} - R_{\text{th\_ch}} \tag{4.26}$$

The following section analyzes the results obtained, varying the number of stages and the quantity of IGBTs connected in parallel.

4.4.4.3 Results

The results obtained from the calculations developed in the previous sections are analyzed below. Four tables are presented, each corresponding to a different number of stages. These tables show the detailed breakdown of losses and their associated efficiency. Additionally, the evolution of thermal viability for each configuration can be observed.

First, the results for a converter design with a single stage are shown:

	Nº STAGES			1 Nº IGBTs IN PARALLEL		1
	8MW			10MW		
POWER LOSSES	5000V 1600A	4000V 2000A	6000V 1333.3A	5000V 2000A	4000V 2500A	6000V 1666.6A
1 IGBT CONDUCTION (W)	8474.72	8131.73	8904.96	9405.36	9646.74	9877.68
TOTAL IGBT CONDUCTION LOSSES (W)	33898.90	32526.94	35619.84	37621.44	38586.96	39510.72
1 IGBT SWITCHING	59058.32	61211.49	59548.59	69245.60	71794.13	68244.10
TOTAL IGBT SWITCHING LOSSES (W)	236233.27	244845.95	238194.37	276982.40	287176.51	272976.40
1 DIODE CONDUCTION (W)	1059.96	1898.09	1121.74	2062.92	2661.27	1530.68
TOTAL DIODE CONDUCTION LOSSES (W)	4239.83	7592.34	4486.96	8251.68	10645.07	6122.72
1 DIODE SWITCHING (W)	4704.51	4919.98	4376.43	6011.66	5928.96	5514.99
TOTAL DIODE SWITCHING LOSSES (W)	18818.03	19679.91	17505.70	24046.65	23715.84	22059.94
TOTAL POWER LOSSES IGBT (KW)	270.13	277.37	273.81	314.60	325.76	312.49
TOTAL POWER LOSSES DIODE (KW)	23.06	27.27	21.99	32.30	34.36	28.18
SUBTOTAL POWER LOSSES (KW)	293.19	304.65	295.81	346.90	360.12	340.67
LOSSES TRANSF, INDUCT & CAPAC (KW)	62.74	65.19	63.30	74.24	77.07	72.90
TOTAL POWER LOSSES (KW)	355.93	369.84	359.11	421.14	437.19	413.57
EFFICIENCY (%)	95.74	95.58	95.70	95.96	95.81	96.03
THERMAL STUDY:						
Rth (h-a) IGBT (K/Kw)	-18.069	-18.108	-18.089	-18.279	-18.322	-18.270
Rth (h-a) DIODE (ºC/W)	0.013	0.010	0.013	0.008	0.007	0.009

Figure 0.4.15: Losses and thermal viability results for a single stage configuration.

As can be seen, this configuration is thermally unviable, causing excessive heating of the IGBTs. On the other hand, the efficiencies are around 96%, a typical value for high-power LLC resonant converters.

Next, the results for eight stages are presented:

	Nº STAGES			8 Nº IGBTs IN PARALLEL		1
	8MW			10MW		
POWER LOSSES	5000V 1600A	4000V 2000A	6000V 1333.3A	5000V 2000A	4000V 2500A	6000V 1666.6A
1 IGBT CONDUCTION (W)	1059.34	1016.47	1113.12	1175.67	1205.84	1234.71
TOTAL IGBT CONDUCTION LOSSES (W)	33898.90	32526.94	35619.84	37621.44	38586.96	39510.72
1 IGBT SWITCHING	7382.29	7651.44	7443.57	8655.70	8974.27	8530.51
TOTAL IGBT SWITCHING LOSSES (W)	236233.27	244845.95	238194.37	276982.40	287176.51	272976.40
1 DIODE CONDUCTION (W)	114.38	134.72	87.25	140.93	172.87	111.78
TOTAL DIODE CONDUCTION LOSSES (W)	3660.14	4311.07	2791.98	4509.62	5531.75	3576.89
1 DIODE SWITCHING (W)	588.06	615.00	547.05	751.46	741.12	689.37
TOTAL DIODE SWITCHING LOSSES (W)	18818.03	19679.91	17505.70	24046.65	23715.84	22059.94
TOTAL POWER LOSSES IGBT (KW)	270.13	277.37	273.81	314.60	325.76	312.49
TOTAL POWER LOSSES DIODE (KW)	22.48	23.99	20.30	28.56	29.25	25.64
SUBTOTAL POWER LOSSES (KW)	292.61	301.36	294.11	343.16	355.01	338.12
LOSSES TRANSF, INDUCT & CAPAC (KW)	62.62	64.49	62.94	73.44	75.97	72.36
TOTAL POWER LOSSES (KW)	355.23	365.86	357.05	416.60	430.98	410.48
EFFICIENCY (%)	95.75	95.63	95.73	96.00	95.87	96.06
THERMAL STUDY:						
Rth (h-a) IGBT (K/Kw)	-7.704	-8.013	-7.863	-9.378	-9.727	-9.310
Rth (h-a) DIODE (ºC/W)	0.138	0.129	0.153	0.107	0.105	0.120

Figure 0.4.16: Losses and thermal viability results for an eight-stage configuration.

The previously analyzed eight-stage converter — with stage powers between 1 and 1.25 MW — also proves thermally unviable. The solution in this case is to increase the number of stages to reduce the

thermal load per device. The results for a configuration with sixteen parallel stages — corresponding to stage powers between 500 and 625 kW — are shown below:

	Nº STAGES			15 Nº IGBTs IN PARALLEL		1
	8MW			10MW		
POWER LOSSES	5000V 1600A	4000V 2000A	6000V 1333.3A	5000V 2000A	4000V 2500A	6000V 1666.6A
1 IGBT CONDUCTION (W)	529.67	508.23	556.56	587.84	602.92	617.36
TOTAL IGBT CONDUCTION LOSSES (W)	33898.90	32526.94	35619.84	37621.44	38586.96	39510.72
1 IGBT SWITCHING	3691.14	3825.72	3721.79	4327.85	4487.13	4265.26
TOTAL IGBT SWITCHING LOSSES (W)	236233.27	244845.95	238194.37	276982.40	287176.51	272976.40
1 DIODE CONDUCTION (W)	56.54	63.70	41.73	66.29	80.73	53.05
TOTAL DIODE CONDUCTION LOSSES (W)	3618.73	4076.70	2670.91	4242.33	5166.52	3395.04
1 DIODE SWITCHING (W)	294.03	307.50	273.53	375.73	370.56	344.69
TOTAL DIODE SWITCHING LOSSES (W)	18818.03	19679.91	17505.70	24046.65	23715.84	22059.94
TOTAL POWER LOSSES IGBT (KW)	270.13	277.37	273.81	314.60	325.76	312.49
TOTAL POWER LOSSES DIODE (KW)	22.44	23.76	20.18	28.29	28.88	25.45
SUBTOTAL POWER LOSSES (KW)	292.57	301.13	293.99	342.89	354.65	337.94
LOSSES TRANSF, INDUCT & CAPAC (KW)	62.61	64.44	62.91	73.38	75.89	72.32
TOTAL POWER LOSSES (KW)	355.18	365.57	356.90	416.27	430.54	410.26
EFFICIENCY (%)	95.75	95.63	95.73	96.00	95.87	96.06
THERMAL STUDY:						
Rth (h-a) IGBT (K/Kw)	4.142	3.524	3.824	0.793	0.096	0.931
Rth (h-a) DIODE (ºC/W)	0.280	0.265	0.312	0.221	0.217	0.247

Figure 0.4.17: Losses and thermal viability results for a fifteen-stage configuration.

	Nº STAGES			20 Nº IGBTs IN PARALLEL		1
	8MW			10MW		
POWER LOSSES	5000V 1600A	4000V 2000A	6000V 1333.3A	5000V 2000A	4000V 2500A	6000V 1666.6A
1 IGBT CONDUCTION (W)	423.74	406.59	445.25	470.27	482.34	493.88
TOTAL IGBT CONDUCTION LOSSES (W)	33898.90	32526.94	35619.84	37621.44	38586.96	39510.72
1 IGBT SWITCHING	2952.92	3060.57	2977.43	3462.28	3589.71	3412.21
TOTAL IGBT SWITCHING LOSSES (W)	236233.27	244845.95	238194.37	276982.40	287176.51	272976.40
1 DIODE CONDUCTION (W)	45.13	50.37	33.08	52.36	63.67	41.98
TOTAL DIODE CONDUCTION LOSSES (W)	3610.45	4029.82	2646.70	4188.87	5093.47	3358.68
1 DIODE SWITCHING (W)	235.23	246.00	218.82	300.58	296.45	275.75
TOTAL DIODE SWITCHING LOSSES (W)	18818.03	19679.91	17505.70	24046.65	23715.84	22059.94
TOTAL POWER LOSSES IGBT (KW)	270.13	277.37	273.81	314.60	325.76	312.49
TOTAL POWER LOSSES DIODE (KW)	22.43	23.71	20.15	28.24	28.81	25.42
SUBTOTAL POWER LOSSES (KW)	292.56	301.08	293.97	342.84	354.57	337.91
LOSSES TRANSF, INDUCT & CAPAC (KW)	62.61	64.43	62.91	73.37	75.88	72.31
TOTAL POWER LOSSES (KW)	355.17	365.51	356.88	416.21	430.45	410.22
EFFICIENCY (%)	95.75	95.63	95.73	96.00	95.87	96.06
THERMAL STUDY:						
Rth (h-a) IGBT (K/Kw)	10.065	9.292	9.667	5.879	5.008	6.051
Rth (h-a) DIODE (ºC/W)	0.352	0.333	0.392	0.279	0.273	0.310

Figure 0.4.18: Losses and thermal viability results for a twenty-stage configuration —final solution—.

In this case, with sixteen parallel stages, the system is thermally viable. However, it is observed that when the charger operates at maximum power, the thermal viability is at its limit. In fact, if fifteen stages were used instead of sixteen, the $R_{\text{th\_ha}}$ values at 10 MW would be negative, indicating unacceptable overheating.

For this reason, the proposed final solution is to use twenty parallel stages. Each stage would provide between 400 and 500 kW, establishing a sufficient thermal margin and ensuring proper operation of the components studied. Moreover, a greater number of stages improves overall thermal management by reducing losses per device and distributing heat dissipation more effectively.

It should be noted that, in practice, megawatt-scale chargers typically consist of 40 to 50 stages. However, this configuration serves a different purpose — supplying multiple vehicles simultaneously, where each stage or group of stages is assigned to a single vehicle.

The distribution of losses and thermal study corresponding to the proposed solution is shown below:

As previously noted, this solution provides an acceptable thermal margin.

Finally, the solution is compared with the alternative of implementing ten stages and two IGBTs in parallel in the switching stage, keeping the current through each IGBT the same:

	Nº STAGES		10	Nº IGBTs IN PARALLEL		2
	8MW			10MW		
POWER LOSSES	5000V 1600A	4000V 2000A	6000V 1333.3A	5000V 2000A	4000V 2500A	6000V 1666.6A
1 IGBT CONDUCTION (W)	423.74	406.59	445.25	470.27	482.34	493.88
TOTAL IGBT CONDUCTION LOSSES (W)	33898.90	32526.94	35619.84	37621.44	38586.96	39510.72
1 IGBT SWITCHING	2952.92	3060.57	2977.43	3462.28	3589.71	3412.21
TOTAL IGBT SWITCHING LOSSES (W)	236233.27	244845.95	238194.37	276982.40	287176.51	272976.40
1 DIODE CONDUCTION (W)	91.09	105.43	68.59	110.07	134.64	87.60
TOTAL DIODE CONDUCTION LOSSES (W)	3643.58	4217.32	2743.55	4402.70	5385.66	3504.15
1 DIODE SWITCHING (W)	470.45	492.00	437.64	601.17	592.90	551.50
TOTAL DIODE SWITCHING LOSSES (W)	18818.03	19679.91	17505.70	24046.65	23715.84	22059.94
TOTAL POWER LOSSES IGBT (KW)	270.13	277.37	273.81	314.60	325.76	312.49
TOTAL POWER LOSSES DIODE (KW)	22.46	23.90	20.25	28.45	29.10	25.56
SUBTOTAL POWER LOSSES (KW)	292.59	301.27	294.06	343.05	354.86	338.05
LOSSES TRANSF, INDUCT & CAPAC (KW)	62.62	64.47	62.93	73.41	75.94	72.34
TOTAL POWER LOSSES (KW)	355.21	365.74	356.99	416.47	430.81	410.39
EFFICIENCY (%)	95.75	95.63	95.73	96.00	95.87	96.06
THERMAL STUDY:						
Rth (h-a) IGBT (K/Kw)	10.065	9.292	9.667	5.879	5.008	6.051
Rth (h-a) DIODE (ºC/W)	0.173	0.163	0.193	0.136	0.133	0.152

Figure 0.4.19: Comparison of the proposed solution —20 stages— with the 10-stage / 2 IGBTs per stage configuration.

As expected, due to the identical current distribution per device, the results are the same. However, in practice, the option with twenty stages would offer better thermal management.

As demonstrated throughout the comparisons, the efficiencies achieved for each operating point are very similar. This is because, to ensure a realistic comparison between scenarios, the same IGBT and diode models have been used in all cases. Since the electrical characteristics of the devices remain constant, increasing the number of stages reduces the current through each component, but simultaneously increases the total number of devices. Consequently, when calculating the total system losses, the results remain practically unchanged.

Furthermore, the efficiencies obtained — around 95% to 96% — fall within the typical range for commercial high-power LLC resonant converters, validating the design.

4.4.5 Economic Study

In this final section, an economic assessment is presented for the cost associated with this very high-power charger.

For the cost estimation, reference was made to information provided by a specialized supplier of high-power charging systems for industrial and electric mobility applications, with experience in commercial megawatt-range solutions.

It is important to emphasize that megawatt-scale chargers represent highly specialized technology, with very few companies worldwide currently developing and commercializing such systems. Moreover, due to the customized nature of these systems, prices are not publicly available, making it difficult to obtain reliable economic benchmarks without direct contact with manufacturers.

Their product catalog highlights two models of high-power chargers. The first, with a maximum power of 400 kW, costs approximately 55,000 euros. The second model, which is of greater relevance to this study, has a maximum power of 1440 kW and costs 268,000 euros.

This second unit — as it falls within the megawatt-scale range — serves as a valid reference for establishing comparisons with the system proposed in this project. The cost per kW for chargers of this caliber is 186.11 euros per kW. Accordingly, the total cost of the 10 MW charger developed in this study would be 1,861,111 euros — that is, one million eight hundred sixty-one thousand one hundred eleven euros.

Furthermore, following direct communication with the supplier, a detailed breakdown of costs by functional system block was obtained, enabling a more precise structuring of the economic analysis of the proposed converter. The cost breakdown of the charger, expressed as percentages, is summarized in the following table:

Table 0.4.6: Total physical system cost breakdown

Component	Percent (%)	Cost (€)
Control electronics	5	93,055.55
Power electronics	35	651,388.85
Electrical wiring	10	186,111.10
Cooling system + liquid cooling hoses	15	279,166.65
Chassis + mounting trays for power stages	13	241,944.43
Electrical protections	4	74,444.44
Sensors and signal acquisition	2	37,222.22
Additional components	16	297,777.76
TOTAL	100	1,861,111

As shown, a section at the end includes additional unspecified components, grouped under that concept as no exact percentage information was available for each of them.

It is necessary to reiterate that the design of certain internal elements of the charger — such as the cooling system, high-current cabling, or the vehicle control structure — is beyond the scope of this project. Additionally, in order to compare it with the other power supply systems studied, the cost of the 2 MWh battery — 247,420 euros, as explained in Section 4.3.4.2 — must be added.

In general terms, it can be stated that the coolant used in this charger should be dielectric oil, as it is a non-conductive liquid, providing greater safety in the event of leaks and allowing closer contact with copper components.

The section concludes with the following findings.

4.4.6 Section Conclusions

This work has developed the complete design of a high-power charger based on LLC resonant architecture, dimensioned to operate in the 8 to 10 MW range. The system was conceived with a modular and scalable approach to ensure both technical feasibility and practical operability for large-scale electric mobility applications.

LTspice simulations validated the expected behavior of the resonant tank, transformer, rectifiers, and output filter, confirming the system's ability to deliver a clean, stable DC signal to the battery with negligible ripple.

Thermal analysis showed that full-load operation with a limited number of stages could compromise device integrity. As a solution, a configuration of 20 parallel stages was proposed, with each delivering 400 to 500 kW, ensuring safe thermal margins for the selected IGBTs and diodes.

Structurally and economically, the system cost was estimated at €1,861,111 through a functional block breakdown. While representing a significant initial investment, this is a considerably more cost-effective option within the scale of Hyperloop budgets compared to the other power supply systems studied. Additionally, high-power chargers have a much more established track record in electric mobility applications than inductive charging or hydrogen fuel cell systems.

A key strategic advantage of the proposed system is the complete externalization of power electronics and charging elements to a fixed station, eliminating the need to carry heavy converters and cooling systems on board. This significantly reduces vehicle weight, improving energy efficiency, range, and operational performance.

Overall, the design represents a viable, efficient, and scalable technical solution for ultra-high-power charging systems, aligned with the requirements of future real-world Hyperloop applications.

4.5 Inductive Power Transfer

The next proposed power supply method for a Hyperloop vehicle is inductive charging.

Inductive charging enables wireless energy transfer through magnetic coupling between a transmitting coil installed along the tube and a receiving coil — the E-Pickup — mounted on the vehicle. This principle, based on Faraday-Lenz's law, generates a variable magnetic flux that induces an AC voltage in the receiver, which is then rectified and converted to DC to power the train systems. In

high-power applications, the primary coil is fed by a high-power inverter operating at frequencies typically between 20 and 60 kHz.

Applying inductive charging to Hyperloop offers significant advantages for high-speed transport. First, it eliminates mechanical friction components inherent to conventional charging systems, reducing wear and maintenance requirements — a critical benefit in continuous, high-speed operation. The system is also insensitive to adverse environmental conditions, such as dust or humidity, enhancing overall reliability.

A key advantage is the ability to minimize on-board system weight. Inductive charging allows all infrastructure — inverters, transmitting coils, and control systems — to be installed along the guideway or at stations, removing the need for heavy on-board storage or generation systems and limiting on-board energy storage to the battery alone.

Additionally, the system can be segmented so that only the transmission sections directly beneath the vehicle are activated.

This section details the operation of this technology and presents the proposed system design. Given the similarities in circuit topology between inductive charging and the charger studied later in this work, the focus is on designing and simulating the E-Pickup system — the receiving coils capable of supplying the necessary energy to the vehicle both at rest and in motion. The analysis discusses and justifies key design values and compares the proposed design with other approaches. A thermal study and an economic analysis are also conducted to evaluate implementation feasibility.

Reference values, dimensions, and technical parameters used in this study were drawn from scientific publications and specialized technical documentation. This approach ensures the analysis remains focused on key design aspects while addressing the complexity inherent to such a system. All selected values were rigorously sourced to guarantee technical feasibility and realistic design within the scope of this project.

4.5.1 Operation Principles of Inductive Charging

Although inductive charging enables on-board battery supply while the vehicle is in motion — which might suggest potential reductions in battery capacity and weight — this is not the case. Due to the strict acceleration requirements outlined in Section 4.2.1 and the need for a 24 MW peak during this phase, the battery capacity must still meet the maximum discharge rate limits defined previously. With the supercapacitor option ruled out, the minimum required battery capacity remains 2 MWh — the same as that considered for the supercharger-based system.

The key distinction between inductive charging and the supercharger lies in the former's ability to operate both in motion and while stationary, whereas the supercharger only allows stationary charging. However, given that the system requires a mandatory stop of 10 to 15 minutes at the end of each trip, no notable differences arise in terms of charging speed or stop time, as the supercharger is designed to fully recharge the battery within this window. The main comparative factors between the two systems are therefore implementation cost, efficiency, and scalability.

The electrical circuit of the inductive charging system is illustrated in the following figure:

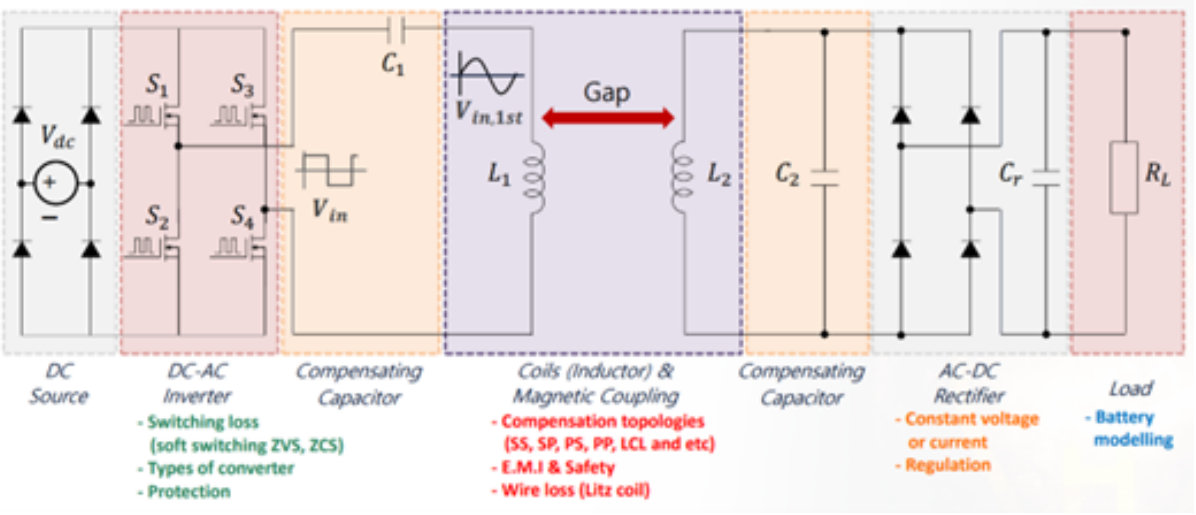

Figure 0.5.1: Electrical circuit of the inductive charging system.

The DC-AC inverter responsible for energizing the inductive charging system is powered by a DC bus, typically obtained through a rectifier connected to the electrical grid or, alternatively, from a large-capacity renewable energy source. The study of the circuitry preceding the inverter, as well as the detailed explanation of the inverter itself, its multistage configuration, and component selection, are beyond the scope of this section, as its operation is analogous to the supercharger design analyzed later.

The system includes a high-power resonant inverter — in the megawatt range — that raises the grid frequency to values between 20 kHz and 60 kHz, in line with various high-power inductive charging studies, where higher frequencies induce greater voltage in the pickups. In this study, 60 kHz is chosen due to the high power requirements to be analyzed later.

Following the inverter are two key elements: the transmitter and the pickup.

The transmitter consists of Litz wire, designed for high-frequency operation, with individually insulated strands to minimize skin effect losses and ensure uniform current distribution across the conductor cross-section. These Litz wire coils are distributed along the route, forming the transmitter array that generates the magnetic field inducing voltage in the vehicle's receivers. To optimize efficiency and avoid unnecessary energy consumption, the transmitter cable is segmented so that only the segment beneath the vehicle is activated at any given time, powered by switching the corresponding inverter. In this study, a coil length of 100 meters is adopted, consistent with typical MAGLEV inductive charging designs [13].

The pickup, or E-Pickup, is positioned according to the rail's location in the Hyperloop system — mounted beneath the train if the rail is below the capsule, or above if the rail is overhead. Each pickup consists of coils, resonance capacitors, an E-shaped core, and a rectifier. Its role is to capture the magnetic field generated by the transmitter and convert it into DC to supply the vehicle's battery system. The E-core enhances magnetic coupling and concentrates flux in the air gap, improving transfer efficiency.

A detailed circuit diagram as applied to a real train is shown below:

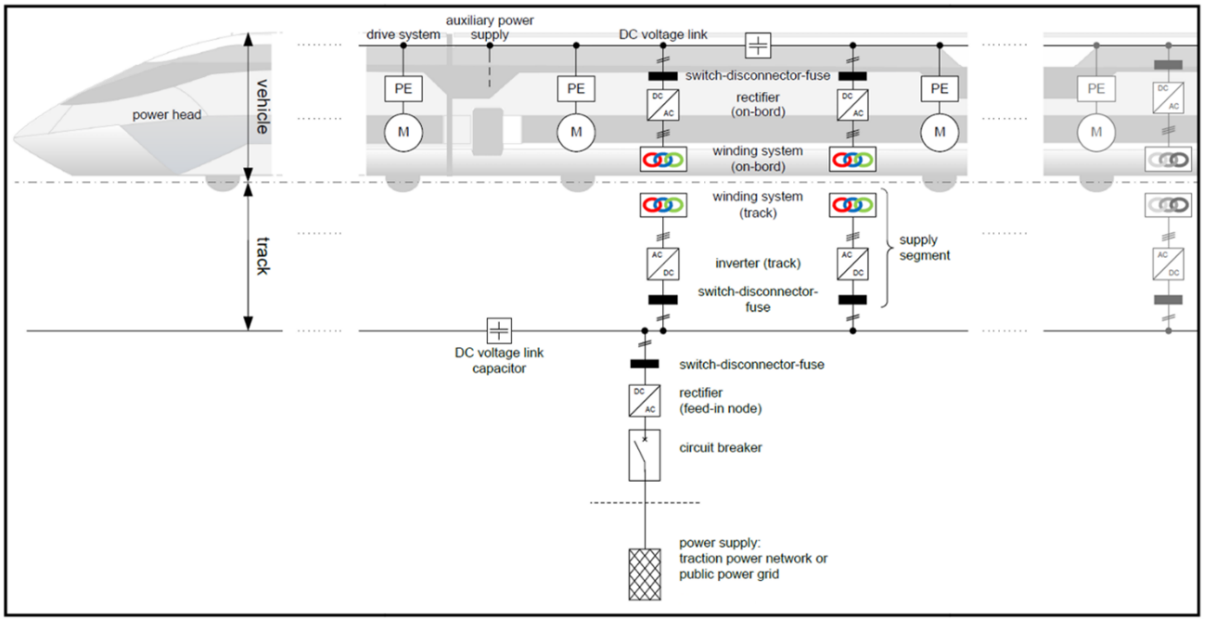

Figure 0.5.2: Inductive charging system applied to a real train.

The next step involves designing and simulating an E-Pickup system capable of reliably supplying the energy required by the vehicle.

4.5.2 Power Requirements for Pickups

The following develops the necessary calculations to quantify the number of pickups and transmitter coils required to meet the system's energy demands.

This study proposes an inductive charging system combining both stationary and in-motion charging. Since each trip ends with a mandatory stop of at least 10 minutes, the energy that can be charged during this time is calculated and subtracted from the total battery capacity — set at 2 MWh. This allows the coils to be dimensioned and the power required during the route to be determined to fully charge the battery.

Given the limited number of companies developing this technology at an industrial level, designing pickups for extremely high powers would lack objectivity. Therefore, following a commercial analysis and discussions with specialized suppliers — essential for the subsequent economic study — the design criterion was set to use pickups with a maximum unit power of 4 kW, consistent with the highest power available in current industrial applications.

To determine the number and arrangement of coils, a Hyperloop vehicle length of 125 meters and cabin width of 2.4 meters were considered, according to the model proposed by Hardt. The pickup design uses a width of 342 mm. Placing seven pickups in a row would cover the total width of 2.4 meters.

Each pickup adopts a maximum length of 1 meter, in line with current commercial criteria. This allows up to 100 rows of 1 meter each along the vehicle, covering 100 of the 125 meters of train length. This length matches that of the primary coil.

The system of seven pickups per row will later be designed and simulated — accounting for the interaction of magnetic fields — to achieve 28 kW per row —seven pickups of 4 kW each—.

With this pickup power, and assuming a general efficiency of 90% per unit, the energy stored during the 10-minute stop would be:

$$E_{\text{est}}\,(\text{kWh}) = P_{\text{est}}\,(\text{kW}) \times t_{\text{est}}\,(\text{h}) \tag{4.27}$$

$$P_{\text{est}} = P_{\text{pickup}}\,(\text{kW}) \times N_{\text{rows}} \times N_{\text{pickups\_row}} \times \eta_{\text{pickup}} \tag{4.28}$$

$$E_{\text{est}}\,(\text{kWh}) = (4 \times 100 \times 7 \times 0.9) \times \frac{10}{60} = 420\,\text{kWh} \tag{4.29}$$

Thus, 420 kWh of energy are stored during the minimum 10-minute stop. Consequently, of the 2 MWh battery capacity, 1580 kWh must be supplied by the inductive charging system over the entire route.

To achieve this, it is proposed to divide the 500 km route into segments of 120 meters each. Each segment will host several parallel transmitter coils, each 100 meters in length. This provides a 10-meter margin on either side, ensuring sufficient spacing between adjacent coils and proper operation.

The number of segments is:

$$N_{\text{segments}} = \frac{L_{\text{track}}\,(\text{m})}{L_{\text{coil}}\,(\text{m})} = \frac{500000}{120} = 4166.66 \approx 4167 \text{ segments} \tag{4.30}$$

The energy to be delivered by each segment is:

$$E_{\text{segment}}\,(\text{J}) = \frac{E_{\text{total}}\,(\text{kWh}) \times 3.6 \times 10^6\,(\text{J/kWh})}{N_{\text{segments}}} = \frac{1580 \times 3.6 \times 10^6}{4167} = 1{,}516{,}800\,\text{J} \tag{4.31}$$

Given that the Hyperloop crosses each coil at a speed of 700 km/h — equivalent to 194.44 m/s — the time to cross a 100-meter coil is:

$$t_{\text{segment}}\,(\text{s}) = \frac{100\,(\text{m})}{194.44\,(\text{m/s})} = 0.514\,\text{s} \tag{4.32}$$

Assuming a 95% efficiency for the resonant inverter, the power required from the inverter is:

$$P_{\text{inverter}}\,(\text{W}) = \frac{E_{\text{segment}}}{t_{\text{segment}} \times \eta} = \frac{1{,}516{,}800}{0.514 \times 0.95} = 2{,}794{,}105\,\text{W} \approx 2800\,\text{kW} \tag{4.33}$$

Finally, the power required per coil is:

$$P_{\text{coil}}\,(\text{kW}) = \frac{P_{\text{inverter}}\,(\text{kW})}{N_{\text{coils}}} = \frac{2794}{700} = 3.99\,\text{kW} \approx 4\,\text{kW} \tag{4.34}$$

4.5.3 Pickup System Design

This section presents the design criteria, operating conditions, and the studies and simulations conducted using JMAG software. These studies include varying the primary current to determine the optimal value for achieving 4 kW per pickup. Additionally, the magnetic flux distribution is analyzed to ensure uniform power induction. The analysis is completed with an efficiency study as a function of airgap and a thermal study of both the primary and pickup cables.

Throughout the studies, 2D geometry images were included to facilitate visual comparison of the different configurations analyzed. However, to achieve the most accurate and realistic results, all calculations were performed using 3D models. This approach also allowed the study of power induction behavior under a simulated pickup motion at 700 km/h.

4.5.3.1 Geometry Analysis

Before defining the final design — consisting of seven pickups each 342 mm wide — various alternatives were studied. The 2.4-meter cabin width of the Hyperloop and the 4 kW limit per pickup constrain the design, requiring a narrow geometry but sufficient height to induce the necessary power, prioritizing the largest possible copper cross-section.

As previously noted, given the limited technical data for applications of this type, two reference designs were initially analyzed. The first is based on a pickup documented in a scientific study for 1 MW inductive charging systems [14]. The second corresponds to the design proposed in a JMAG application note, used as a base for inductive charging pickup simulations [9]. From these references, the final model adopted in this study was developed — optimized to maximize induced power, increase the effective copper cross-section, and meet the width constraints set for the vehicle.

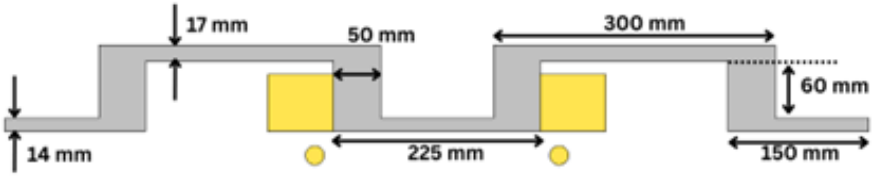

Figure 0.5.3: Reference pickup geometry based on the 1 MW inductive charging system study [14].

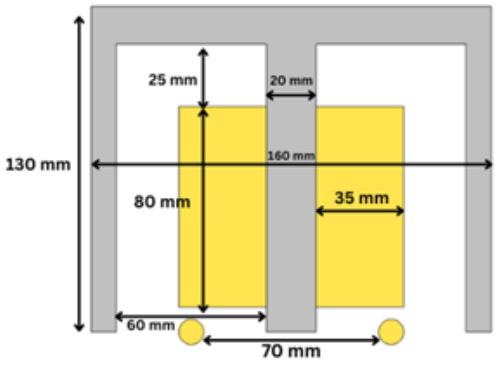

Figure 0.5.4: Reference pickup geometry from JMAG application note simulation [9].

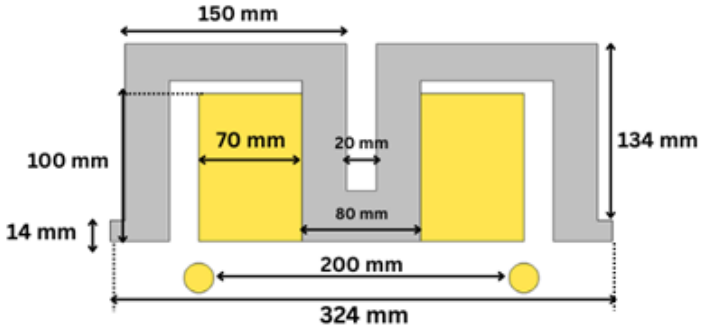

Figure 0.5.5: Final pickup geometry adopted in this study, optimized for the Hyperloop vehicle.

When simulating the different pickups and their associated system, it is necessary to define the key operating parameters.

For the primary coil, or transmitter, a 30 mm diameter Litz wire with five turns per coil was considered. This value was adopted based on a scientific study on Inductive Power Transfer —IPT— systems, where such a design is specified to handle up to 400 A [14]. The equivalent circuit used in JMAG for the transmitter is shown below:

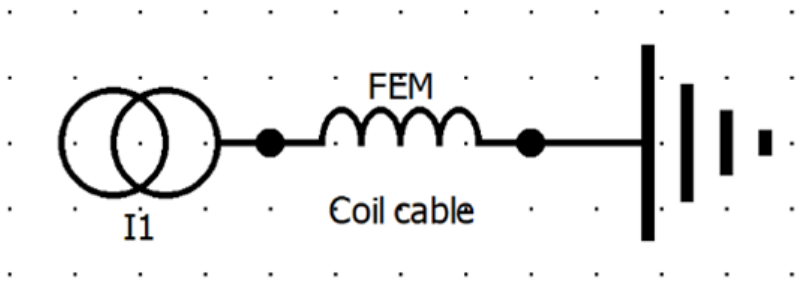

Figure 0.5.6: Equivalent circuit of the transmitter coil used in JMAG simulation.

As shown, the primary coil circuit consists of a three-phase power supply at the operating frequency of 60 kHz, with current varied for the studies. The coil includes the number of turns and its internal resistance, with values detailed later.

The system of seven pickups in a row is represented by the following diagram:

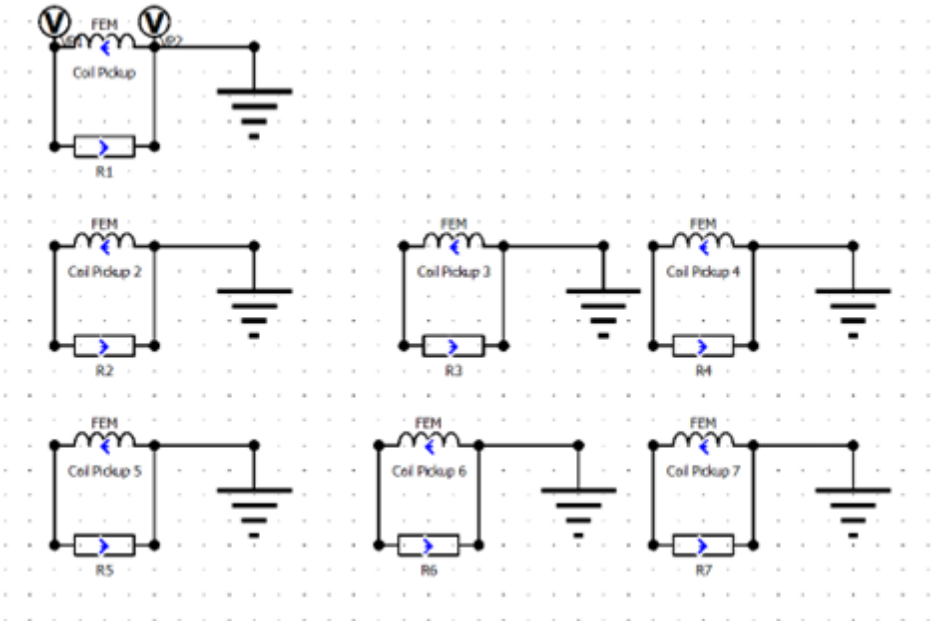

Figure 0.5.7: Equivalent circuit of the pickup system used in JMAG simulation.

This schematic represents each pickup coil, including its internal resistance and number of turns, as well as a parallel resistance modeling the battery supplied by the system.

A preliminary comparison of the induced power for each model is shown in the following graph:

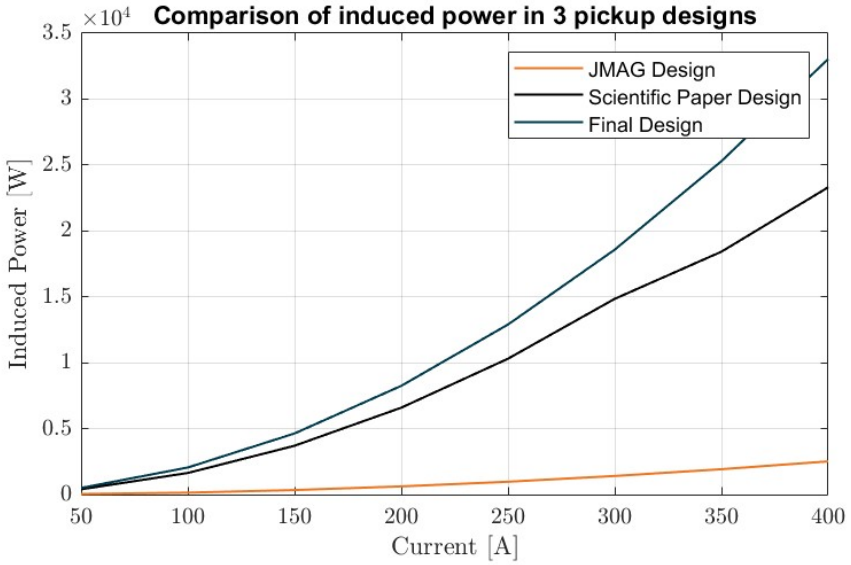

Figure 0.5.8: Comparison of induced power for different pickup designs.

The final design exhibits significantly higher induced power compared to the other two designs for the same current and circuit values, confirming it as the optimal design for this study.

However, it is important to note that the power values obtained are not entirely representative when considering the practical feasibility of the system. As discussed earlier, one critical design factor is the high cost associated with Litz wire. The previously shown 2D image of the final design illustrates two wires for a single primary coil — one outgoing section and one return section. While implementing a primary coil for each pickup would ensure maximum force induction per unit, the cost of cable required to cover 500 kilometers makes this option economically unviable.

Therefore, the behavior of a system consisting of seven pickups powered by a reduced number of primary coils was analyzed, studying the impact on the induced magnetic flux and captured power as a function of the configuration adopted.

4.5.3.2 Key Parameters Calculation

To provide a clearer representation of the key parameters defining the system and to enhance the validity of the results, the figure below shows the final arrangement of the primary coils and the seven-pickup system:

Figure 0.5.9: Final arrangement of the three primary coils and the seven-pickup system.

As shown, the final wiring design consists of three primary coils, marked in the 2D representation with a circle at the current exit point and a cross at the current entry point. Each coil is 310 mm wide and spaced 400 mm apart.

The 3D representation of the final design — used for the various calculations and simulations presented in this section — is shown below:

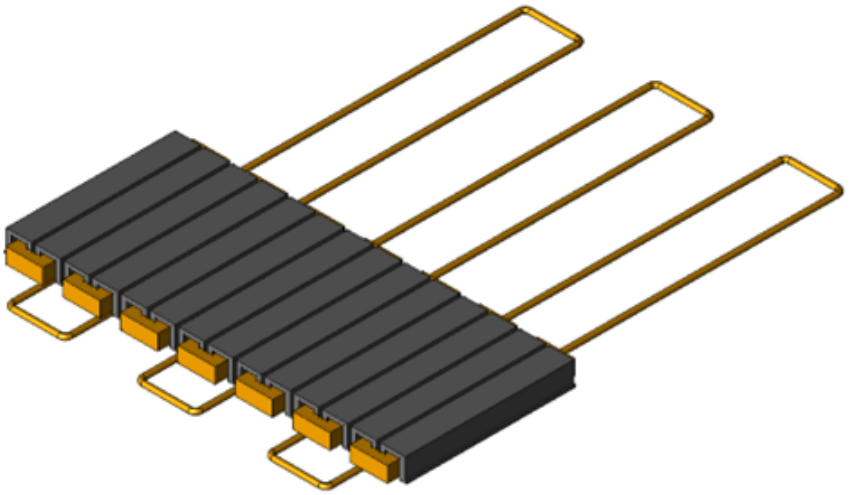

Figure 0.5.10: 3D representation of the final pickup and primary coil design used in simulations.

It is important to note that, to reduce simulation times, a 3-meter coil was modeled instead of the actual 100-meter length, assuming the effective power induced by the pickups remains constant along their entire passage over the coil.

A crucial first parameter to analyze is the electrical resistance of the primary cable, calculated as follows:

$$R = \frac{\rho L}{A} \tag{4.35}$$

Where:

- R: cable resistance —Ω—
- ρ: material resistivity —Ω·m— in this case copper, with $\rho = 1.673 \times 10^{-8}$ Ω·m —the only value available in JMAG—
- L: total cable length —m—
- A: cable cross-sectional area —m^2—

For the primary cable, a total diameter of 30 mm —15 mm radius— and 5 turns was defined. This implies a 3 mm radius per turn. Given that the coil is 100 meters long and 310 mm wide, the perimeter or length per coil is:

$$P_{\text{coil}}\,(\text{m}) = 2 \times 100\,\text{m} + 0.31\,\text{m} = 200.62\,\text{m} \tag{4.36}$$

Thus, the resistance of the primary cable, considering three coils connected in series, is:

$$R_{\text{primary}} = \frac{P_{\text{coil}} \times N_{\text{turns}} \times N_{\text{coils}} \times \rho}{A} = \frac{200.62 \times 5 \times 3 \times 1.673 \times 10^{-8}}{0.003^2} = 1.7806\,\Omega \quad (4.37)$$

For the different configurations studied, the resistance was recalculated accordingly. The example detailed here corresponds to the final proposed configuration and serves as the reference case.

Moving on to the pickup analysis: the cable design includes 12 turns per pickup, which maximizes the effective copper area and ensures sufficient induced current, while balancing the available space and required number of turns.

The arrangement of the turns within the pickup coil is illustrated in the following figure:

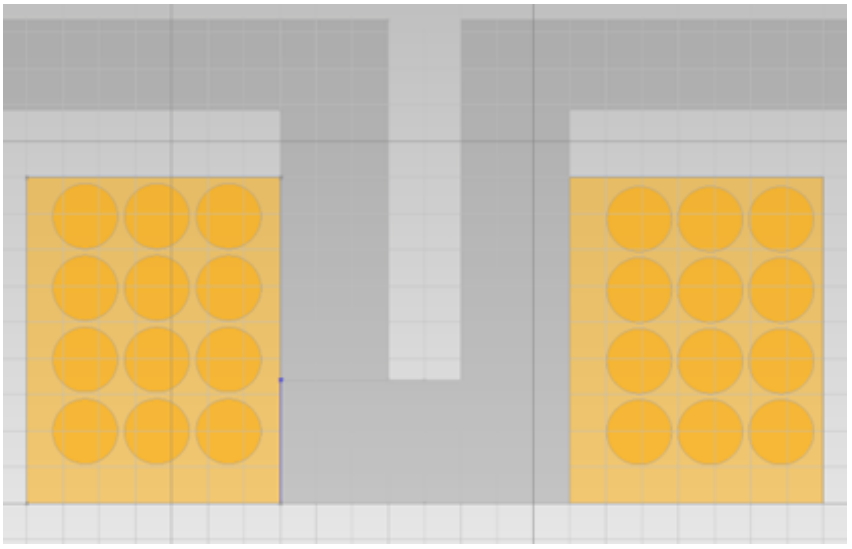

Figure 0.5.11: Arrangement of the turns within the pickup coil.

In this configuration, a cable diameter of 18 mm was selected based on high-power IPT design references. Additionally, an insulation thickness of 0.6 mm and a 0.6 mm gap between cables were specified.

Since each pickup forms an independent circuit, and given an average coil width of 150 mm and a length of 1 meter, the total coil perimeter is determined as:

$$P_{\text{coil}}\,(\text{m}) = 2 \times L_{\text{coil}}\,(\text{m}) + W_{\text{coil}}\,(\text{m}) = 2 \times 1 + 0.15 = 2.30\,\text{m} \quad (4.38)$$

And, the resistance of the cable of each pickup is:

$$R_{\text{pickup}} = \frac{P_{\text{coil}} \times N_{\text{turns}} \times \rho}{A\,(\text{m}^2)} = \frac{2.30 \times 12 \times 1.673 \times 10^{-8}}{0.009^2} = 0.04536\,\Omega \quad (4.39)$$

After having deduced the determination of these parameters, the inverse process is carried out to analyze how the optimal arrangement was reached.

4.5.3.3 Design Configuration Evaluation

To determine the arrangement and number of cables that would maximize the induced power under the same current conditions — without exceeding 4 kW per pickup — several design scenarios were evaluated.

A nominal airgap of 15 mm was adopted, in line with Hardt's proposal for a real Hyperloop vehicle. Later, an efficiency study will examine power transmission performance as the airgap varies.

The first scenario considered using a single, wider primary coil, as illustrated in the figure:

Figure 0.5.12: Single primary coil configuration considered in the first design scenario.

This option was then compared — under identical operating conditions and with adjusted primary resistance values — to configurations using three coils — the final selected design — and seven coils:

Figure 0.5.13: Three primary coil configuration —final design—.

Figure 0.5.14: Seven primary coil configuration evaluated for comparison.

The graph below compares the induced power for the three configurations at different primary currents:

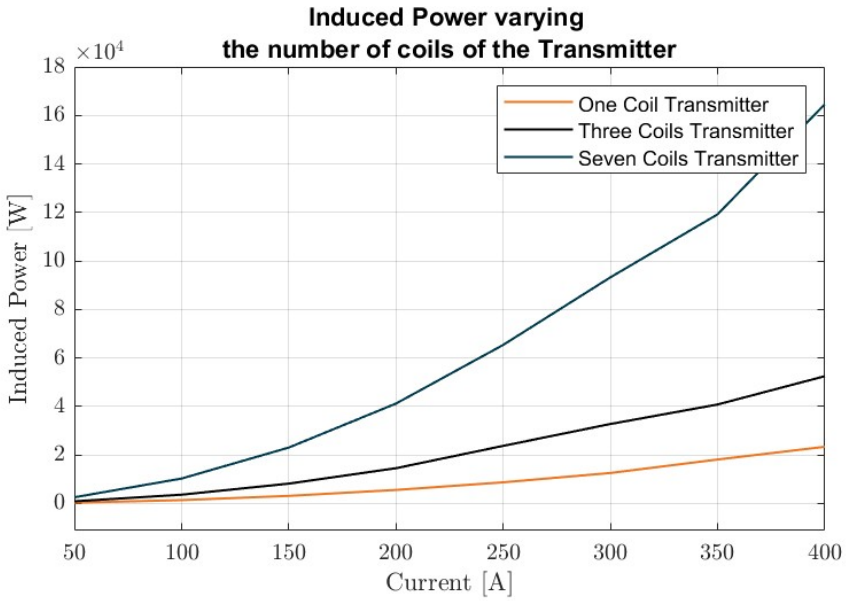

Figure 0.5.15: Induced power as a function of primary current for different coil configurations.

As noted earlier, the goal is to achieve a total power of 28 kW, evenly distributed across the seven pickups, which can be reached in the range of 250 A to 300 A with the three-coil primary system —black curve—. In contrast, this power level could not be achieved with a single coil, even at 400 A, thus ruling out that design option.

For a transmitter composed of seven coils, the desired power could be reached with currents between 150 A and 200 A. However, the high cost of the required Litz wire — analyzed in the subsequent economic study — makes this alternative unfeasible.

From an economic standpoint, using a single primary coil would be the most favorable option. However, due to the small airgap, this solution induces very high power only in the pickups located directly above the coil, leaving the others underutilized and failing to reach the total power required by the system. In contrast, the proposed solutions with three or seven primary coils achieve a more uniform power distribution among all pickups, allowing each to operate around its nominal 4 kW power.

A diagram of the magnetic flux generated by the cables and induced in the pickups is shown below. The flux lines reveal the power distribution across the pickups:

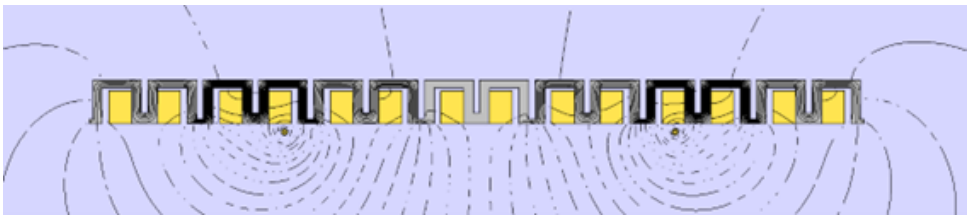

Figure 0.5.16: Magnetic flux distribution with a single primary coil.

In the single-coil case, it is clear how significant current is induced in the pickups closest to the cables, while those farther away operate at much lower power levels than nominal.

This issue is fully addressed with the seven-coil primary system:

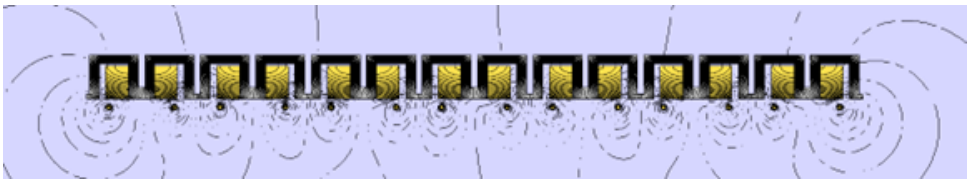

Figure 0.5.17: Magnetic flux distribution with seven primary coils.

As can be seen, the flux distribution is completely uniform, as each pickup effectively has its own transmitter coil, ensuring balanced magnetic coupling.

Finally, the magnetic flux diagram for the selected final design with three coils is presented:

Figure 0.5.18: Magnetic flux distribution for the three-coil primary system —close view—.

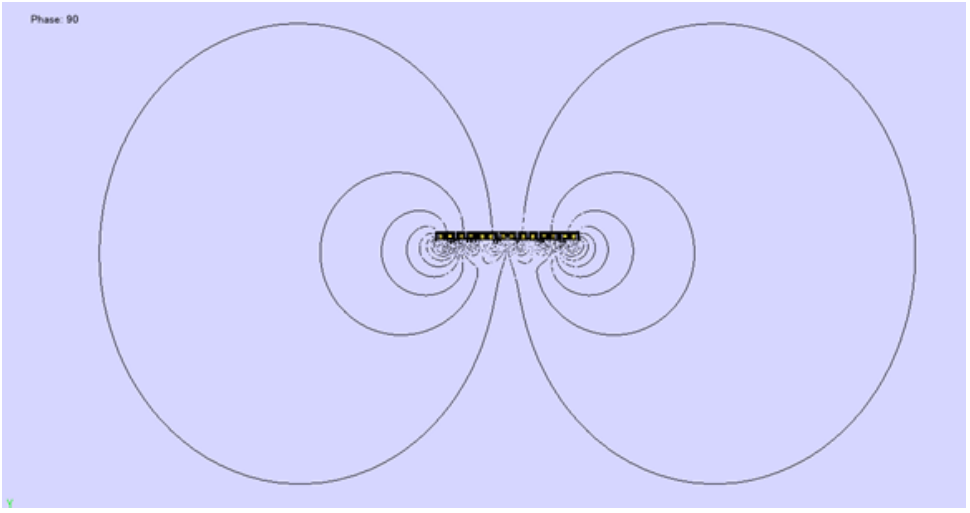

Figure 0.5.19: Magnetic flux distribution for the three-coil primary system —far view—.

The flux distribution is nearly homogeneous thanks to the arrangement of the three primary coils. By spacing the coils optimally, the design prevents pickups from operating significantly above or below their nominal power, thereby maximizing the usable power of each unit.

Additionally, with seven coils, having so many closely spaced coils carrying high currents can lead to the emergence of electromagnetic forces between cables — although these would be mechanically secured — or proximity effects, where the magnetic fields of adjacent conductors induce parasitic currents in neighboring wires when large AC currents are present.

Based on the goal of optimizing a primary system formed by three coils, two alternative layout options are presented next:

Figure 0.5.20: Three-coil configuration with 200 mm and 400 mm cable spacings.

Figure 0.5.21: Three-coil configuration with equidistant cable layout.

In both layout options, the entry and exit cables of each coil are equidistant, so that the distance between cables within the same coil matches the spacing between adjacent coils, as illustrated in the 2D representation.

A comparative graph of the induced power for the three studied alternatives is presented:

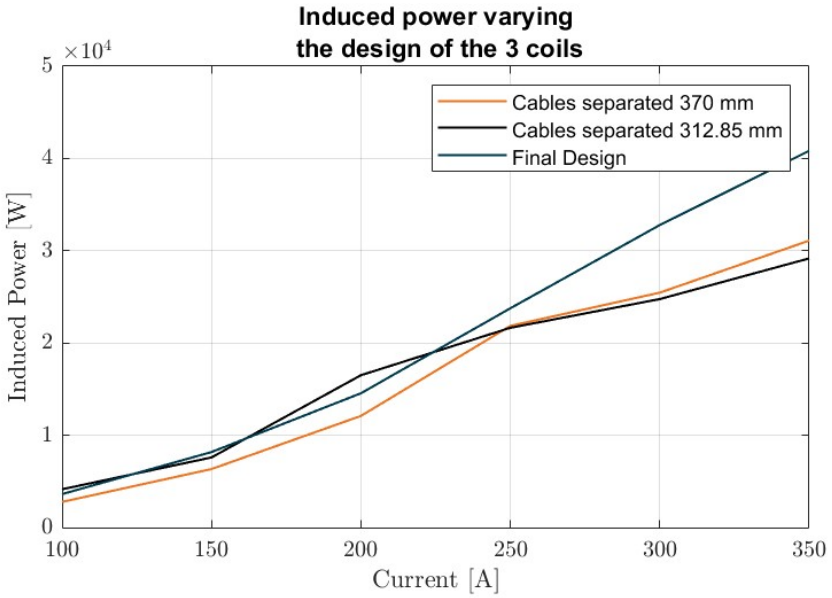

Figure 0.5.22: Induced power as a function of distance between primary cables for different three-coil configurations.

From the results, it is concluded that the final selected design offers the best balance between applied current and the number of primary coils, optimizing the induced power across the entire system.

With this design established, it is essential to determine the precise current the inverter must supply to induce the required 28 kW in the pickup system. The evolution of induced power as a function of primary current, in the range of 250 A to 300 A at 60 kHz, is depicted below for the final design:

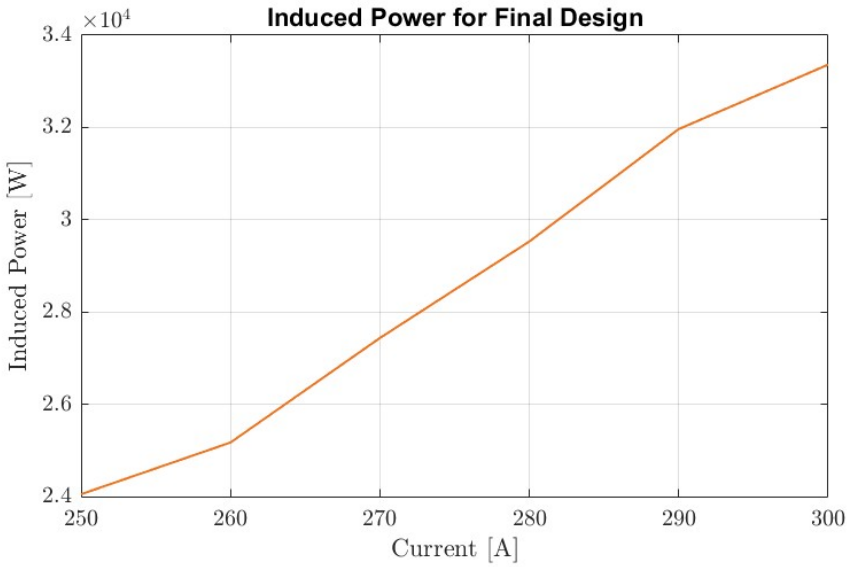

Figure 0.5.23: Induced power as a function of primary current for the final three-coil design.

As shown, approximately 273 A achieves the 28 kW of induced power needed for the pickup system. This value, combined with the homogeneous power distribution achieved by the final design, ensures the system meets the total energy demand required to supply the vehicle.

Next, the efficiency of the inductive charging system at different airgap values — the separation between pickups and primary coils — is analyzed. Efficiency is defined as the ratio of power induced in the pickups to the active power supplied by the primary coil assembly. The results are illustrated in the following graph:

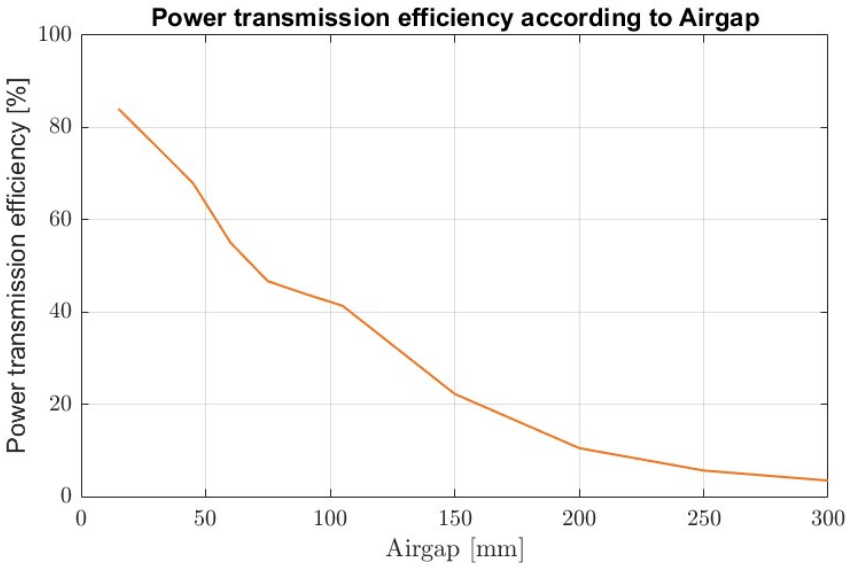

Figure 0.5.24: Efficiency of the inductive charging system as a function of airgap distance.

The graph analysis reveals a clear decline in power transmission efficiency as the distance between the primary coils and the pickups increases. Magnetic flux dispersion becomes significant even at small separations, highlighting that in this technology, maintaining a minimal gap between the transmitter and receiver is critical.

For the final design studied, the system achieves an efficiency of 84%. It is important to note that the majority of the system's apparent power is reactive power. JMAG enables extraction of the active power supplied by the inverter to the cable, which in turn feeds the pickups. To deliver the previously calculated 2.8 MW from the inverter, the system requires an operating voltage of approximately 10,000 V.

Finally, a thermal study was conducted, analyzing the temperature evolution of the primary coils and the pickups. In the case of the pickups, this analysis is less critical, as a commercial 4 kW model — designed for safe continuous operation at nominal power — was used as a reference, and its thermal behavior was therefore not plotted.

The temperature rise of the primary coils over 10 seconds is depicted in the following graph:

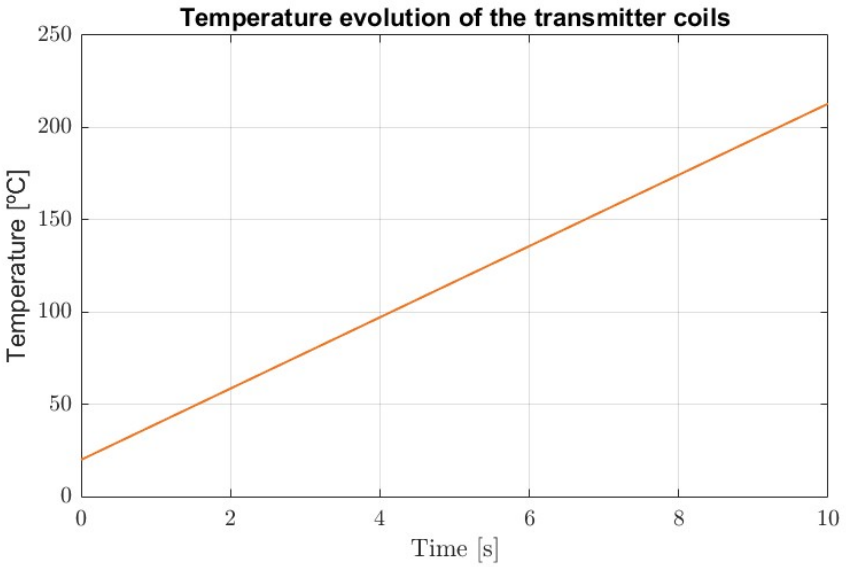

Figure 0.5.25: Temperature rise of the primary coils over 10 seconds of operation.

From these results, as previously mentioned, the primary coil is active for only about 0.514 seconds — the time it takes for the vehicle to pass over each coil. Under these conditions, starting from an initial temperature of 20 ºC, the temperature rise during that interval is approximately 11.7 ºC. Even if the system were activated one or two seconds earlier, the maximum temperature reached would not compromise the safety of the Litz cable insulation.

4.5.4 Economic Study

The economic study of the proposed inductive charging system is developed below. Given the limited number of companies commercially developing this technology, direct contact was established with a specialized supplier to obtain reference data for budgeting the pickups and the required Litz cable. This allowed for a realistic economic analysis consistent with the current state of the technology.

One of the main costs of this technology is the high-power inverters that supply the transmitter coils. As noted in the introduction, the inductive charging system must be segmented along the route, activating only the transmission sections directly beneath the vehicle.

In conventional rail systems, substations that supply electric trains via pantographs are located at intervals of 50 kilometers. Similarly, this study assumes 10 substations spaced at this distance, with each inverter supplying the transmitter coils within its corresponding range [5].

The cost of a 35 kW high-frequency inverter is €25,630, equivalent to €732.28 per kW. When scaling to the power required by this study's inverter, and considering economies of scale, the cost

per kW is likely to fall within €200 to €400. For a realistic estimate, an average of €300 per kW was adopted. This leads to a total inverter cost of:

$$\text{Inverter cost} = 300 \frac{}{\text{kW}} \times 2800\,\text{kW} = 840\,000 \tag{4.40}$$

The enclosure for housing the inverter is additionally estimated at €3,000.

Regarding the Litz cable, the cost is €18.80 per meter. The total required length must be calculated. First, connections from the inverters to the respective transmitter coils are considered a straight longitudinal line along the vehicle's direction — approximately 500 km. Additionally, there are 4167 primary coil systems, each consisting of 3 coils of 200.62 meters. This results in a total required Litz cable length of:

$$L_{\text{total}} = 500{,}000 + 4167 \times 200.62 = 500{,}000 + 2{,}505{,}551.4 = 3{,}005{,}551.4\,\text{m} \tag{4.41}$$

In the primary transmission system, capacitor modules must be installed for each coil to compensate for reactive power. These capacitors are essential given the long distances supplied by the inverters, as the lines present distributed inductance and capacitance that significantly increase reactive power.

Finally, the system includes the pickups themselves —E-Pickups— along with their respective power regulators.

The total cost of all these elements — comprising the technology needed to implement an inductive charging system capable of powering a Hyperloop — is summarized in the following table:

Table 0.5.1: Inductive Power Transfer System Costs

Elements	Quantity	Unit	Price (€)	Amount (€)
Inductive Power Supply 2.8 MW	10	ea	840,000	8,400,000
Box IPPC	10	ea	3,000	30,000
Litz Cable	3,005,551.4	m	18.8	56,504,366.32
Capacitor Module	4,167	ea	699	2,912,733
E-pickup 4 kW	700	ea	548	383,600
Inductive Power regulator 4 kW	700	ea	2,434	1,703,800
TOTAL	-	-	-	69,934,499.32

As can be observed, the economic study of the main components of the proposed inductive charging system amounts to approximately seventy million euros.

It should be noted that additional costs still need to be accounted for, such as the supports and guidance systems for the primary cables, labor costs, additional electronics to be installed on the

vehicle, and other complementary elements. Nevertheless, this study includes the primary components that make up this technology, for which pricing is known with certainty, thereby allowing the required investment to make this concept a reality to be quantified.

Each pickup weighs 8.4 kg, and each power regulator weighs 4.1 kg. With a total of 700 units of each on board the vehicle, and adding the weight of the 2 MWh battery — 22,222.2 kg — the total additional weight the vehicle must carry is calculated as:

$$\text{Total additional weight (kg)} = 8.4\times700+4.1\times700+22{,}222.2 = 5{,}880+2{,}870+22{,}222.2 = 30{,}972.2\,\text{kg} \tag{4.42}$$

Finally, the operational cost of this technology is estimated at €111 per trip, the same as calculated in Section 4.3.3.2 for the battery-only option, since the energy consumed ultimately corresponds to the 2 MWh energy demand of the route.

4.5.5 Section Conclusions

The analysis carried out demonstrates that inductive charging is a technically viable option for powering a real Hyperloop vehicle, offering significant advantages such as the ability to fully externalize the weight of the power system — placing the infrastructure along the route — and thus minimize on-board weight. This optimizes vehicle performance and simplifies its structural design. It is a modular and scalable system, with independent segments that can be activated only beneath the train, facilitating maintenance and component replacement in case of failure. Furthermore, the absence of physical contact means mechanical wear is virtually nonexistent, reducing maintenance needs compared to other technologies. Finally, the system enables the vehicle to be powered both in motion and during mandatory stops, ensuring full recharging within the planned timeframes. Throughout the study, a system of E-Pickups and primary coils was designed and simulated in JMAG, optimizing geometry, number of turns, layout, and primary current to meet power requirements. The system's performance was validated in terms of induced power, magnetic flux, efficiency, and thermal behavior, ensuring a technically consistent design. However, the main drawback is the cost, which is approximately seventy million euros — significantly higher than the other power supply methods studied. While it is a mature technology at smaller scales, its implementation in a system like Hyperloop still requires overcoming economic and optimization challenges to become viable on a large scale.

Chapter 5

Conclusions

The conducted study has made it possible to analyze and compare three potential solutions for the power supply system of a real Hyperloop vehicle, aimed at meeting a high and demanding energy requirement — around 2 MWh per trip, with peak power reaching 24 MW during acceleration. This comparison has been addressed from multiple perspectives, including additional on-board weight, infrastructure cost, operational cost, technological maturity, and scalability of each proposal.

Regarding on-board weight, a clear difference is observed among the various solutions. Alternatives that rely solely on a battery as the on-board energy source — such as the system powered by a supercharger or inductive charging — present lower additional weight. In contrast, hydrogen-based hybrid systems incorporate tanks and fuel cells that significantly increase the total vehicle weight, potentially impacting dynamic performance and overall efficiency. This can be seen in the additional on-board weight table, which clearly illustrates these differences:

Table 0.0.1: Additional Weight on Vehicle (kg)

Solution	**Additional Weight (kg)**
H2 24 MW	45,220.1
H2 18 MW	35,994.0
H2 12 MW	31,452.1
H2 6 MW	27,121.1
Supercharger	22,222.2
Inductive Power Transfer	30,972.2

In terms of infrastructure cost, all three options involve initial investments typical of a large-scale project like Hyperloop. However, the technologies based on superchargers or hydrogen entail more contained infrastructure costs, while inductive charging requires a significantly higher investment, a direct consequence of the complexity of the installation and the materials used. This is reflected in the infrastructure cost table:

Table 0.0.2: Infrastructure Cost (€)

Solution	Cost (€)
H2 24 MW	949,192
H2 18 MW	738,444
H2 12 MW	574,004
H2 6 MW	422,131
Supercharger	2,108,531
Inductive Power Transfer	70,181,919

In terms of operational cost, the differences between solutions are significant. Alternatives that use rechargeable batteries as the main on-board energy source stand out for their low operational cost, as they rely on electricity supplied by the grid. In contrast, the hydrogen hybrid system involves a much higher cost per trip due to reactant consumption, which could have a greater economic impact during prolonged operation. This aspect is reflected in the operational cost table:

Table 0.0.3: Operational Cost (€)

Solution	Total Cost Per Trip (€)	Total Cost 2200 Trips (€)
H2 24 MW	2,179.17	4,794,173.0
H2 18 MW	2,183.39	4,803,450.9
H2 12 MW	1,679.20	3,694,231.2
H2 6 MW	1,116.12	2,455,458.3
Supercharger	111.0	244,288.0
Inductive Power Transfer	111.0	244,288.0

From the perspective of technological maturity, the supercharger relies on high-power technologies that are already under development and testing for commercial applications, giving it a high level of maturity. Inductive charging, although well established in low-power applications, is still at an earlier stage regarding its adaptation to megawatt-scale high-speed systems. The hydrogen-battery hybrid system presents an intermediate level, with solutions proven in other types of transport but requiring adaptation to the specific environment of Hyperloop.

Finally, scalability is a key factor in the future development of these technologies. The resonant LLC multistage supercharger stands out for its modular integration capability and its basis in high-power technology already advancing through commercial development, facilitating adaptation to different vehicle types or networks and allowing installed power to be adjusted as needed. Inductive charging, in addition to its theoretical potential for contactless supply, offers the advantage of a modular architecture, where multiple lower-power commercial elements can be combined to provide the necessary energy, opening the door to scalable and flexible solutions if technological

and standardization challenges are overcome. In the case of the hydrogen-battery hybrid system, its scalability depends on the ability to modulate the installed power and tank size, though progress is needed in optimizing fuel cell power density and reducing costs to make it competitive for Hyperloop applications.

Overall, this work represents a significant contribution to advancing knowledge about power supply systems applicable to Hyperloop, providing an objective and comparative foundation for evaluating different technological alternatives. The study of power supply systems is not a secondary aspect; it is a fundamental pillar that will determine the technical, economic, and operational viability of this new form of transport. The ability to design efficient, scalable, and safe energy solutions will be key to transforming the Hyperloop concept into a functional and sustainable reality. Only through the development of energy systems capable of meeting Hyperloop's demands can its full potential as a mobility system of the future be realized. This analysis reinforces the need for continued research in this field, driving innovation and directly contributing to the progress of a technology that could mark a milestone in the history of transportation.

References

[1] Botella de oxígeno medicinal 50 litros. Accessed: 2025-04-19.

[2] H2.live - hydrogen prices in europe. Accessed: 2025-04-19.

[3] Omie monthly report march 2025. Accessed: 2025-04-19.

[4] Sam Abdel-Rahman. Resonant llc converter: Operation and design. Technical Report AN 2012-09, Infineon Technologies North America (IFNA) Corp., 2012. Design example and figures from Infineon application note.

[5] Federal Railroad Administration. Ice trainset inspection and maintenance plan. Technical report, Federal Railroad Administration (FRA), 1993.

[6] Apilados. El hidrógeno como gas real: factor de compresibilidad, 2022. Accessed: 2025-06-17.

[7] Battery University. Lithium-titanate battery (lto): A better choice for high current equipment, 2025. Accessed April 2025.

[8] BloombergNEF. Lithium-ion battery pack prices hit record low of $139/kwh, 2020.

[9] JSOL Corporation. Power transmission analysis of a wireless power transfer system. Technical report, JSOL Corporation, 2015. JMAG Application Note.

[10] Wendell Cox and Joseph Vranich. California high-speed rail: An updated due diligence report, 2013. Page 72, Endnote 17.

[11] Diesel Progress North American Edition. Several studies on regenerative braking efficiency, 2025. Accessed April 2025.

[12] Hardt Hyperloop. Hyperloop system description, 2025. Accessed April 2025.

[13] S. Jeong, J. Kim, J.W. Kim, and S. Lee. Design of 100 kw high power wireless charging system for a high-speed train. *Journal of Electrical Engineering & Technology*, 2012. Accessed for MAGLEV inductive charging design, Figure 10.

[14] Jae Hee Kim, Byung-Song Lee, Jun-Ho Lee, Seung-Hwan Lee, Chan-Bae Park, Shin-Myung Jung, Soo-Gil Lee, Kyung-Pyo Yi, and Jeihoon Baek. Development of 1-mw inductive power transfer system for a high-speed train. *IEEE Transactions on Industrial Electronics*, 62(10):6242–6250, 2015.

[15] M. López. *Analysis of hydrogen fuel cell powerplant architectures for future transport applications*. PhD thesis, Universitat Politècnica de València, Valencia, 2022. Doctoral Thesis directed by R. Novella Rosa, September 12th, 2022.

[16] Quantum Spain. Botella de oxígeno medicinal 50 litros.

[17] Dynex Semiconductor. Calculating power losses in an igbt module. Technical Report AN6156, Dynex Semiconductor, 2021.

[18] ON Semiconductor. Design and application guide for high-power llc resonant converters. Technical Report TND6318/D, ON Semiconductor, 2016. Figure 10 table, approximate values.

[19] Spear Power Systems. Lithium-ion chemistries, 2021. Accessed April 2025.

[20] Steelhead Composites. Steelhead composites hydrogen storage tank copv brochure 1001. Available upon request or from manufacturer documentation.

[21] Trane. Solution plus - dxpa product catalog, 2025. Accessed April 2025.

[22] U.S. Department of Energy. Onboard hydrogen storage cost and performance status 2019, 2019.

[23] U.S. Department of Energy. Automotive fuel cell targets status 2020, 2020.

[24] Wikipedia contributors. Compressibility factor, 2024. Accessed: 2025-06-17.

Bibliography

[1] Botella de oxígeno medicinal 50 litros. Accessed: 2025-04-19.

[2] H2.live - hydrogen prices in europe. Accessed: 2025-04-19.

[3] Omie monthly report march 2025. Accessed: 2025-04-19.

[4] Sam Abdel-Rahman. Resonant llc converter: Operation and design. Technical Report AN 2012-09, Infineon Technologies North America (IFNA) Corp., 2012. Design example and figures from Infineon application note.

[5] Federal Railroad Administration. Ice trainset inspection and maintenance plan. Technical report, Federal Railroad Administration (FRA), 1993.

[6] Apilados. El hidrógeno como gas real: factor de compresibilidad, 2022. Accessed: 2025-06-17.

[7] Battery University. Lithium-titanate battery (lto): A better choice for high current equipment, 2025. Accessed April 2025.

[8] BloombergNEF. Lithium-ion battery pack prices hit record low of $139/kwh, 2020.

[9] JSOL Corporation. Power transmission analysis of a wireless power transfer system. Technical report, JSOL Corporation, 2015. JMAG Application Note.

[10] Wendell Cox and Joseph Vranich. California high-speed rail: An updated due diligence report, 2013. Page 72, Endnote 17.

[11] Diesel Progress North American Edition. Several studies on regenerative braking efficiency, 2025. Accessed April 2025.

[12] Hardt Hyperloop. Hyperloop system description, 2025. Accessed April 2025.

[13] S. Jeong, J. Kim, J.W. Kim, and S. Lee. Design of 100 kw high power wireless charging system for a high-speed train. *Journal of Electrical Engineering & Technology*, 2012. Accessed for MAGLEV inductive charging design, Figure 10.

[14] Jae Hee Kim, Byung-Song Lee, Jun-Ho Lee, Seung-Hwan Lee, Chan-Bae Park, Shin-Myung Jung, Soo-Gil Lee, Kyung-Pyo Yi, and Jeihoon Baek. Development of 1-mw inductive power transfer system for a high-speed train. *IEEE Transactions on Industrial Electronics*, 62(10):6242–6250, 2015.

[15] M. López. *Analysis of hydrogen fuel cell powerplant architectures for future transport applications*. PhD thesis, Universitat Politècnica de València, Valencia, 2022. Doctoral Thesis directed by R. Novella Rosa, September 12th, 2022.

[16] Quantum Spain. Botella de oxígeno medicinal 50 litros.

[17] Dynex Semiconductor. Calculating power losses in an igbt module. Technical Report AN6156, Dynex Semiconductor, 2021.

[18] ON Semiconductor. Design and application guide for high-power llc resonant converters. Technical Report TND6318/D, ON Semiconductor, 2016. Figure 10 table, approximate values.

[19] Spear Power Systems. Lithium-ion chemistries, 2021. Accessed April 2025.

[20] Steelhead Composites. Steelhead composites hydrogen storage tank copv brochure 1001. Available upon request or from manufacturer documentation.

[21] Trane. Solution plus - dxpa product catalog, 2025. Accessed April 2025.

[22] U.S. Department of Energy. Onboard hydrogen storage cost and performance status 2019, 2019.

[23] U.S. Department of Energy. Automotive fuel cell targets status 2020, 2020.

[24] Wikipedia contributors. Compressibility factor, 2024. Accessed: 2025-06-17.

HYPERLOOP **UPV**

Shaping the future